

A SPECTROSCOPIC SURVEY OF FIELD RED HORIZONTAL-BRANCH STARS

MELIKE AFŞAR^{1,2}, ZEYNEP BOZKURT¹, GAMZE BÖCEK TOPCU¹, DANA I. CASETTI-DINESCU^{3,4,5}, CHRISTOPHER SNEDEN²,
AND GIZEM ŞEHİTOĞLU¹

¹Department of Astronomy and Space Sciences, Ege University, 35100 Bornova, İzmir, Turkey; melike.afsar@ege.edu.tr, zeynep.bozkurt@ege.edu.tr, gamzebocek@gmail.com

²Department of Astronomy and McDonald Observatory, The University of Texas, Austin, TX 78712, USA; afsar@astro.as.utexas.edu, chris@verdi.as.utexas.edu

³Department of Physics, Southern Connecticut State University, 501 Crescent Street, New Haven, CT 06515, USA; danacasetti@gmail.com

⁴Astronomical Institute of the Romanian Academy, str. Cutitul de Argint 5, Bucharest, Romania

⁵Radiology and Biomedical Imaging, Yale School of Medicine, 300 Cedar Street, New Haven, CT 06519

ABSTRACT

A metallicity, chemical composition, and kinematic survey has been conducted for a sample of 340 candidate field red horizontal branch stars. High resolution, high signal-to-noise spectra were gathered with the McDonald Observatory 2.7m Tull and the Hobby-Eberly Telescope echelle spectrographs, and were used to determine effective temperatures, surface gravities, microturbulent velocities, [Fe/H] metallicities, and abundance ratios [X/Fe] for seven α and Fe-group species. The derived temperatures and gravities confirm that at least half of the candidates are true RHB stars, with (average) parameters $T_{\text{eff}} \sim 5000$ K, $\log g \sim 2.5$. From the α abundances alone the thin and thick Galactic populations are apparent in our sample. Space motions for 90% of the program stars were computed from Hipparcos and Gaia parallaxes and proper motions. Correlations between chemical compositions and Galactic kinematics clearly indicate the existence of both thin and thick disk RHB stars.

Keywords: stars: abundances – stars: atmospheres – stars: evolution – stars: horizontal-branch

1. INTRODUCTION

Red horizontal branch stars (RHBs) are core-helium-burning stars that have evolved beyond the red giant branch (RGB). They reside on the horizontal branch (HB) between red clump stars (RCs) – the redder counterparts of the RHB stars – and the instability strip. The location of stars on the HB is mainly affected by the dependency of H-burning efficiency on the envelope mass (Salaris & Cassisi 2006): the higher the envelope mass the redder the location of the star on the HB. Other parameters such as He abundance, metallicity, age, initial stellar mass and rotation also play important roles on the HB star locations. Although RHBs can be easily identified in color-magnitude diagrams (CMD) of globular clusters (GC), it is more challenging to distinguish them in the field since they can be easily confused with the subgiant (SG) phases of high-mass former main-sequence (MS) stars. Field RHBs are relatively rare and have not been paid enough attention in the literature. In spite of the identification challenges, field RHB stars are very important tools in many aspects. They can be used for distance determinations as standard candles, similar to RCs (e.g. Stanek et al. 1998; Udalski 2000; Alves et al. 2002; Laney et al. 2012; Hawkins et al. 2017, and references therein). Their kinematic and abundance distributions throughout the Galaxy can provide valuable information on the chemical evolution of our Galaxy (e.g. Chen et al. 2010, 2011; Shi et al. 2012). Most importantly, they are the dig sites where light element nucleosynthesis and mixing products lead to surface abundance changes. Several studies including Rose (1985) and Gilmore & Reid (1983) investigated the kinematics of field RHBs as a group and concluded that they are members of the thick disk component of the Galaxy.

Chemical compositions for some of the thick disk RHBs have been studied in detail by, e.g., Tautvaisiene (1996, 1997) and Tautvaišienė et al. (2001). In Afşar et al. (2012) (hereafter ASF12) we reported the first systematic stellar parameter and chemical composition study of field stars with temperatures and luminosities consistent with the location of the HR diagram red horizontal branch but without stellar population assignment. After analysis of spectroscopic data for about 80 stars with weakly-constrained color-magnitude diagram (CMD) positions near the RHB domain, ASF12 suggested that 18 were probable true RHBs, which they defined as those with effective temperatures $4900 \text{ K} < T_{\text{eff}} < 5500 \text{ K}$, surface gravities $2.2 \lesssim \log g \lesssim 2.8$, and carbon isotopic ratios $^{12}\text{C}/^{13}\text{C} \leq 30$. Interestingly,

the kinematics of these 18 stars suggested that 13 of them belong to the thin disk, while only five of them have space motions consistent with the Galactic thick disk membership. The metallicities of the thin disk RHBs were found to be essentially solar, while the thick disk stars are somewhat metal-poor. Thus ASF12 suggested that a low velocity, high metallicity “thin disk” RHB population can sometimes be found in the same RHB domain normally populated by thick disk, mildly metal-poor stars.

With an RHB sample of only 18 stars ASF12 could not draw general conclusions about the relative prevalence of thin- and thick-disk members. Therefore we have gathered high-resolution spectra of more than 300 additional RHB candidates, and here we explore the metallicities, some abundance ratios, and space velocities of this more robust statistical sample. The elements included in this paper are limited to those that can be easily analyzed from equivalent width measurements (Si, Ca, Ti, Cr, Fe, and Ni). In §2 we describe selection of the new targets. Details of observations and spectrum reductions appear in §3. We assemble stellar parallax information in §4, leading to a color-magnitude diagram for our program stars, and in §5 we compute space velocities and estimate Galactic orbital parameters. Spectroscopic atmosphere parameters are described in §6, and derived abundances in §7. In §8 and §9 we investigate relationships between the chemical composition and kinematic information in our RHB sample. Our results are discussed in §10. A second paper (Afşar et al. 2018) will consider abundances of the CNO group and other elements that require iterative synthetic spectrum computations, and will discuss in detail the evolutionary status of the program stars.

2. THE STELLAR SAMPLE

In Table 1 we give basic data for our RHB candidate stars: coordinates, broad-band magnitudes, interstellar medium (ISM) extinction and reddening estimates, spectral types, and the telescope/instrument combination that was used for each star. Simplifying the RHB candidate names as much as possible, we have preferentially adopted the Hipparcos (HIP) catalog number if available, or the Bonner Durchmusterung (BD) number. Some fainter stars have neither of these designations, so we mostly used their Tycho Catalog (TYC) or Two Micron All-Sky Survey (Cutri et al. 2003, 2MASS J, abbreviated here to simply J) numbers. Finally, for a handful of stars, we adopted their single SIMBAD (Wenger et al. 2000) designations from either the HST Guide Star Catalog (GSC) or the Weistrop (1983) (Weis) photometric survey.

To compile a complete list of RHB candidates, we mainly adopted the following criteria by making use of the results from ASF12 and Kaempf et al. (2005) (and references therein):

- $1.5 \lesssim V - K \lesssim 2.2$ (when a K magnitude was available)
- $0.5 \lesssim B - V \lesssim 1.0$
- $-0.5 \lesssim M_V \lesssim 1.5$ (when a parallax was available)
- $\log g < 3.5$ (when a parallax was available)

To assemble a list of RHB candidates based on these criteria, we first started with the Hipparcos catalog. Since observations were obtained with two different telescopes and their echelle spectrographs at McDonald Observatory, the 9.2m Hobby-Eberly Telescope (HET) and the 2.7m Harlan J. Smith Telescope (HJS) (see next section), we had to restrict the apparent magnitudes (V) considering the brightness limitations of these setups: $11 < V < 14$ for the 9.2m HET and $V < 11$ for the 2.7m HJS. Following ASF12 we made use of $B - V$ and $V - K$ colors during the selection of our targets. For the present study we focused more on the $V - K$ color because it is less dependent on metallicity and gravity than is $B - V$, and therefore gives more reliable initial temperature estimates. RHBs mainly reside in the $V - K$ range of ≈ 1.5 – 2.2 (ASF12). $B - V$ colors were taken into account only for the candidates without K magnitude information.

Besides broad-band B , V and K magnitudes, we also used Hipparcos parallaxes, literature spectral types, and Galactic coordinates to find likely RHB field star candidates for spectroscopic observations. Parallaxes were used to determine the preliminary absolute magnitudes to find out whether the absolute magnitudes of stars reside in the adopted selection criteria. Spectral types were limited to the loci of the RHB stars in the H-R diagram (as described in §1, also see ASF12). We also selected candidates with high Galactic latitudes in cases where lack of parallax information. We considered a wide Galactic coordinate range to achieve a more complete sample without bias on stellar population.

We were able to calculate the absolute magnitudes (M_V) for stars with parallaxes (no extinction information was included in assembling the preliminary RHB target list). The absolute magnitude range for RHB stars is approximately

$-0.5 \lesssim M_V \lesssim 1.5$ (e.g. [Kaempf et al. 2005](#)). This restriction helped us to eliminate many stars with magnitudes suggestive of main sequence membership ($M_V \gtrsim 4.0$). We also used a method suggested by [Berdyugina & Savanov \(1994\)](#) in order to estimate preliminary surface gravities of our candidates. Their Eq. 1 relates gravity ($\log g$) to M_V , metallicity $[\text{Fe}/\text{H}]^1$ and effective temperature (T_{eff}) by comparing the observed and predicted equivalent widths of MgH lines in subgiants and giants. The equation is independent of stellar mass and provides good approximations to $\log g$ (within 0.35 dex in case of our sample). For the candidates without parallaxes and $V - K$ colors, we relied on the $B - V$ colors and Galactic latitude information to provide rough $\log g$ estimates. 45 stars that were identified as evolved stars from ASF12 are also included in the present sample (see §6). Six of our program stars were observed twice (see next section). About 370 stars were observed during this project and 340 of them had sufficient data quality to be analysed.

3. OBSERVATIONS, REDUCTIONS, SPECTRUM MEASUREMENTS

From 2011 to 2014 we obtained high resolution, high signal-to-noise (S/N) spectra of our program stars with echelle spectrographs of two telescopes located at McDonald Observatory.

For the majority of targets we employed the 2.7m HJS and its Robert G. Tull Cross-Dispersed Echelle spectrograph ([Tull et al. 1995](#)). Data were acquired in several observing runs dedicated to this program. The instrumental setup was identical to that used by ASF12. Briefly, the combination of echelle grating, camera, and a $1''2$ width entrance slit yielded a spectral resolving power of $R \equiv \lambda/\Delta\lambda \approx 60,000$. The total wavelength coverage was $\lambda\lambda$ 3400-10900, encompassing 63 echelle spectral orders. These orders overlap in wavelength from the blue wavelength limit until $\lambda \simeq 5900 \text{ \AA}$, and small spectral gaps exist for the redder spectral orders.

For some targets we employed the 9.2m HET and its High Resolution Spectrograph (HRS; [Tull 1998](#)). These data were obtained in queue observing mode by the HET staff in individual time slots that depended on the larger HET scheduling matrix, rather than on specifically scheduled nights. The instrumental setup was identical to that used by [Böcek Topcu et al. \(2016\)](#). There are two CCD detectors in this instrument to achieve large spectral coverage. The wavelength ranges were 5100–6900 \AA on the “blue” detector and 7000–8800 \AA on the “red” detector. The spectral resolving power was $R \simeq 60,000$.

The S/N (per resolution element) values calculated near 6900 \AA were taken from the night reports of HET observations (please also see [Böcek Topcu et al. 2016](#)). The S/N values of 2.7m HJS spectra were calculated in a similar manner as described in [Böcek Topcu et al. \(2015\)](#). Overall, the S/N values in the extracted spectra were high, averaging ~ 170 for the whole sample, often $\gtrsim 300$, and rarely < 100 .

Out of our total stellar sample of 340 target stars, six were observed on two different occasions: HIP 4197, HIP 62325, HIP 71837, and HIP 72631 (twice with the 2.7m telescope), and HIP 54858 and HIP 74058 (once each with the 2.7m and HET). These duplicate observations are considered as separate target stars in order to assess the repeatability of our analyses.

We reduced the spectra with IRAF’s² *ccdproc* task: bias subtraction, frame trimming, flat-fielding, and scattered light subtraction. The HET/HRS “blue” and “red” frames were treated as individual observations at all reduction stages. To remove most single-exposure radiation event anomalies, we combined all available integrations for each star into a single reduced frame. IRAF *echelle* package tasks were used for the remaining data reduction steps, beginning with spectral order extraction from the reduced data frames. Th-Ar comparison lamp exposures were used for wavelength calibration. With the IRAF *telluric* task, spectra of hot rapidly rotating stars obtained along side of the target star spectra were used to remove telluric O_2 and H_2O line contamination.

We followed [Böcek Topcu et al. \(2015, 2016\)](#) in measuring the radial velocity (RV) shifts of our targets with the cross-correlation technique in IRAF’s *fxcor* task ([Fitzpatrick 1993](#)). This method compares the spectrum of interest with a template. We elected to create an artificial spectrum with model atmospheric parameters of a typical warm giant ($T_{\text{eff}} = 4900 \text{ K}$, $\log g = 2.5$, $[\text{Fe}/\text{H}] = 0.0$, $\xi_t = 1.2 \text{ km s}^{-1}$). The synthetic spectrum wavelength range was 5020–5990 \AA . The resulting observed RV s were transformed into heliocentric values with IRAF’s *rvcorrect* task. They are listed in Table 2.

We derived spectroscopic values of atmospheric parameters (T_{eff} , $\log g$, ξ_t , $[\text{Fe}/\text{H}]$), and abundance ratios $[\text{X}/\text{Fe}]$ for many neutral and ionized species through analyses of their equivalent widths (EW s). The lines chosen for study will be discussed in §6. To measure EW s we used an Interactive Data Language (IDL) routine developed by [Roederer et al.](#)

¹ We adopt the standard spectroscopic notation ([Wallerstein & Helfer 1959](#)) that for elements A and B, $[\text{A}/\text{B}] \equiv \log_{10}(\text{N}_\text{A}/\text{N}_\text{B})_\star - \log_{10}(\text{N}_\text{A}/\text{N}_\text{B})_\odot$. We use the definition $\log \epsilon(\text{A}) \equiv \log_{10}(\text{N}_\text{A}/\text{N}_\text{H}) + 12.0$, and equate metallicity with the stellar $[\text{Fe}/\text{H}]$ value.

² IRAF is distributed by the National Optical Astronomy Observatory, which is operated by the Association of Universities for Research in Astronomy (AURA) under a cooperative agreement with the National Science Foundation.

(2010) and Brugamyer et al. (2011). This code interactively matches observed line profiles with computed Gaussian line profiles in most cases, or Voigt profiles for some strong lines, recording both EW s (for model parameter and abundance determinations) and central line depths (for initial temperature estimates). In ASF12 we showed that EW s determined from 2.7m spectra for two RHB stars were consistent with their EW s reported in the literature. In Figure 1 we compare EW s for two program RHB stars, HIP 54858 and HIP 74058, measured on our 2.7m and HET spectra. They are in accord with less than 2 mÅ average difference between the two data sets.

4. STELLAR PARALLAXES AND ABSOLUTE MAGNITUDES

Parallax data for our program stars were taken from those obtained by the astrometric space missions Hipparcos (van Leeuwen 2007)³ and Gaia (Gaia DR1 data archive⁴, Gaia Collaboration et al. 2016a,b; Lindegren et al. 2016)⁵. Among our 340 program stars, 159 have parallaxes reported by both surveys, 66 have only Gaia parallaxes, 84 have only Hipparcos parallaxes, and just 31 (9%) have neither.

In Figure 2 we compare the Gaia and Hipparcos parallaxes for our RHB stars. For visual clarity we have chosen plotting axis limits that exclude HIP 113747, for which the Hipparcos parallax is negative. We also have not extended the axis limits to include HIP 19302 and HIP 62325, which have much larger parallaxes than the rest of the sample (Table 2). The Gaia and Hipparcos parallax values are in excellent agreement for both of these stars: for HIP 19302 $\pi_{\text{Gaia}} = 22.27 \pm 0.48$ mas, $\pi_{\text{Hip}} = 22.68 \pm 0.34$ mas, and for HIP 62325 $\pi_{\text{Gaia}} = 22.41 \pm 0.59$ mas, $\pi_{\text{Hip}} = 22.15 \pm 0.35$ mas. In order to avoid clutter in Figure 2 we have chosen to display only representative parallax uncertainties. We have shown the mean Gaia and Hipparcos parallax uncertainties for our RHB stars for Hipparcos parallax bins centered at 1, 3, 5, 7, and 9 mas, with bin widths of 2 mas. The uncertainties for Hipparcos parallaxes increase substantially as their values decrease; the lower limit for reliable parallaxes in that survey is being reached. For Gaia the opposite trend is seen: the larger parallaxes are more uncertain than the smaller ones. This is simply an apparent magnitude effect, as those RHB's with larger Gaia parallaxes are approaching the brightness limit of the Gaia first data release.

Inspection of Figure 2 shows that for large parallaxes the Gaia values agree with the Hipparcos ones, but the Gaia parallaxes are systematically higher at the smallest Hipparcos parallaxes. Arbitrarily dividing the sample into larger and smaller parallax parts, for $\pi_{\text{Hip}} \geq 3$ mas we have $\langle \Delta\pi \rangle = \langle \pi_{\text{Gaia}} - \pi_{\text{Hip}} \rangle = 0.08 \pm 0.09$ mas ($\sigma = 0.80$ mas, 84 stars). For stars with $\pi_{\text{Hip}} < 3$ mas, neglecting those with negative Hipparcos values, $\langle \Delta\pi \rangle = 1.02 \pm 0.12$ mas ($\sigma = 1.03$ mas, 72 stars). There are only eight stars with $\pi_{\text{Hip}} < 3$ mas that do not have Gaia parallaxes. Moreover, the mean Gaia parallax uncertainties are less than the Hipparcos ones at all parallax values. A similar but more comprehensive discussion has been made by Lindegren et al. (2016) for a much larger sample ($\simeq 86\,000$ stars). They adopted a much more rigorous approach and compared Hipparcos and Gaia (Gaia DR1) parallaxes for stars in common. Their effort yielded an actual parallax uncertainty estimate of 1.218 mas. Given the limits of sample size and spectral/evolutionary type of our sample, we regard that uncertainty results as roughly comparable, but the Lindegren et al. value is probably more representative of the true sigma. Therefore for subsequent computations we will adopt Gaia values when available, only using the Hipparcos values when necessary.

Calculations of absolute magnitudes were straightforward for targets with measured parallaxes: $M_V = -5\log(1/\pi) + 5 + V - A_V$, (π in arcsec). About 42% of our stars lie at distances within 200 pc and nearly 47% are within 500 pc. Most of these stars should suffer little ISM extinction. We searched the literature for specific reddening or extinction estimates, and in Table 1 we quote the literature A_V and $E(B - V)$ values when available, or ones computed from one of these quantities using the standard relation $E(B - V) = A_V/3.1$.

The target RHB list was composed several years before the first Gaia data release, and it included RHB candidates that had only rough absolute magnitude estimates. Now aided by Gaia parallaxes we have been able to produce a reliable CMD of the observed RHB sample. In Figure 3 we correlate the $B - V$ colors, corrected for reddening when available, with derived values of M_V . This figure recreates Figure 1 of Kaempf et al. (2005), zoomed in to better show the RHB domain in CMD. Our target stars and those of the (mostly low metallicity) RHB sample of Behr (2003) are displayed along with stars of the Hipparcos catalog (van Leeuwen 2007). The polygon delineated with solid lines shows the whole RHB domain defined by Kaempf et al.. The dashed vertical line splits the RHB region into “blue” and “red” parts, with the blue side covering the more easily identified RHB members. Such stars are substantially bluer than Pop I solar metallicity RC stars, occupying the He-burning RHB domain clearly seen in mildly metal-poor

³ <https://www.cosmos.esa.int/web/hipparcos>

⁴ <https://gea.esac.esa.int/archive/>

⁵ <http://sci.esa.int/gaia/>

globular clusters such as NGC 104 (47 Tuc, [Hesser et al. 1987](#)), NGC 6366, NGC 6624, NGC 6637, and NGC 6838 ([Rosenberg et al. 2000b,a](#)). The red part of the [Kaempf et al.](#) RHB domain is bounded on the cool side by the solid line (or more conservatively the dashed line) that runs parallel to the RGB branch. They argue, based on kinematic information, that the great majority of stars in the area between the slanting dashed and solid lines should also be RHB stars, not RC stars. Adopting their RHB definition in $B - V$, M_V space, we find that a large majority of our targets ought to be RHB stars.

Some of the points that are not in the RHB box in [Figure 3](#) appear to be normal MS, SGB, RGB stars, mostly resulting from stellar distances that have large uncertainties. The target RHB stars without parallax information (thus not plotted in [Figure 3](#)) are on average much fainter than those with parallaxes: they have $\langle V \rangle \simeq 12.0$ while the entire RHB target sample has $\langle V \rangle \simeq 8.5$. If these stars are RHBs ($M_V \sim 0$) and if they suffer no extinction, then they should lie at $\langle d \rangle \simeq 2,500$ pc. But that distance implies substantial reddening if the targets are in the Galactic disk. Therefore RHB assignment for such stars will depend entirely on the spectroscopic model atmosphere parameter derivation to be described in [§6](#).

5. SPACE VELOCITIES AND GALACTIC ORBITAL ELEMENTS

To calculate the space velocities we used proper motions from the Gaia first data release ([Lindgren et al. 2016](#)) when available, else from the Hipparcos revised catalog ([van Leeuwen 2007](#)). With these data and distances taken from the same studies ([§4](#)), and our RV measurements ([§3](#)), we computed U , V , and W space velocities as described in ASF12. The basic equations for these velocity components and their uncertainties were taken from [Johnson & Soderblom \(1987\)](#). These values are with respect to the Sun’s motion, and so we shifted them to local standard of rest (LSR) velocities U_{LSR} , V_{LSR} , and W_{LSR} by adopting the solar peculiar motion with respect to the LSR recommended by [Dehnen & Binney \(1998\)](#): $(U, V, W)_{\odot} = (+10.00, +5.25, +7.17)$ km s $^{-1}$.

In [Figure 4](#) we summarize these velocities in a so-called Toomre diagram ([Sandage & Fouts 1987](#)), which correlates the Galactic rotational velocity V with the quadratic sum of the disk radial velocity with respect to the Galactic center U and the motion out of the plane with respect to the Galactic pole W . Dotted lines in the figure denote constant total space velocity $V_{\text{tot}} = (U_{\text{LSR}}^2 + V_{\text{LSR}}^2 + W_{\text{LSR}}^2)^{1/2}$. The solid black line denotes $V_{\text{tot}} = 180$ km s $^{-1}$. This is approximately the Galactic velocity dividing line between the disk and halo stars (e.g., [Nissen 2004](#)).

Our 309-star sample (the ones with the parallax information) has only 10 with $V_{\text{tot}} > 180$ km s $^{-1}$. These stars are named in [Figure 4](#), along with their $[\text{Fe}/\text{H}]$ metallicities derived in this study ([§6](#)). All but one of these high-velocity stars have $[\text{Fe}/\text{H}] < -0.6$, and most have $[\text{Fe}/\text{H}] \lesssim -1$. Two more low metallicity stars with $V_{\text{tot}} < 180$ km s $^{-1}$ are also labeled in the figure. These stars, HIP 79518 and HIP 52817 have Galactic disk velocities with exceptionally low metallicities. They are of secondary interest to our study, and will not be featured in the remainder of this paper.

For the rest (vast majority) of our sample, the Toomre diagram with velocity limits that encompasses disk members only is given in [Figure 5](#). In ASF12, we assigned stars as “transition objects” that had total velocities $50 < V_{\text{tot}} < 70$ km s $^{-1}$. With the advantage of a larger sample in this study, we examined our stars in chemo-kinematic plane. This revealed that about 86% of our stars in the $50 < V_{\text{tot}} < 70$ km s $^{-1}$ velocity domain have $[\alpha/\text{Fe}] \lesssim +0.13$ and $[\text{Fe}/\text{H}] \gtrsim -0.5$ (see [§7.2](#)). More than 90% of the stars with $V_{\text{tot}} < 50$ km s $^{-1}$ also fall into this $[\text{Fe}/\text{H}]$ and $[\alpha/\text{Fe}]$ range. Therefore, we assign all stars with $V_{\text{tot}} < 70$ km s $^{-1}$ to the kinematic thin disk, absorbing the former transition region in this category. This choice is in accord with earlier studies, e.g., [Loebman et al. \(2011\)](#), [Nissen & Schuster \(2009\)](#), and [Venn et al. \(2004\)](#). The stars in the velocity range $70 < V_{\text{tot}} < 180$ km s $^{-1}$ are thereby designated as thick disk members. [Figure 5](#) shows that our sample populates nearly the whole disk velocity domain, with good representation out to $V_{\text{tot}} \sim 150$ km s $^{-1}$. There are 215 kinematically-defined thin disk stars, 80 thick disk stars, 10 halo stars, and 35 objects with no kinematic information.⁶

Orbital elements were calculated using a 3-component, analytic potential of the Milky Way as in [Dinescu et al. \(1999\)](#). Uncertainties in these elements were determined via Monte Carlo tests in which the initial conditions were varied based on the uncertainties in the measured parallaxes, proper motions and radial velocities. Upper and lower values of these orbital elements are representative of 1-sigma errors (e.g., using the 68% interval centered on the median; see [Casetti-Dinescu & Girard \(2016\)](#)). We will discuss the relationships between kinematics, chemical compositions, and orbital elements: z -component of the angular momentum (L_z); total orbital energy (E_{tot}); eccentricity (e); Galactocentric distance (R_m), in [§9](#).

⁶ The following stars were not included in the kinematic calculations: TYC 23-155-1, because it has a small parallax with an error close to its parallax value; BD+54 2710, because it has a parallax error bigger than its parallax value; and GSC 01227-00508 and J02221759+5710055, which have no proper motion information.

6. MODEL ATMOSPHERIC PARAMETERS

6.1. Initial Estimates

To derive model atmospheric parameters we used a semi-automated iterative software code that was developed by Hollek et al. (2011), Roederer et al. (2014), and refined for our work by Böcek Topcu et al. (2015, 2016). This approach begins with opening estimates for T_{eff} from available broad-band photometry and from temperature-sensitive ratios of line depths in our spectra. Initial “physical” $\log g$ values are calculated from the mean of these temperatures and absolute magnitudes either derived from parallax measurements or estimated roughly from temperatures and assumptions that the stars are evolving along the red giant branch of typical field stars. Beginning model metallicity values were defined as solar, $[M/H] = 0$, and beginning microturbulent velocities were set as $\xi_t = 1.0 \text{ km s}^{-1}$ for stars with $T_{\text{eff}} > 5000 \text{ K}$ (probably main sequence or subgiant), 1.5 km s^{-1} for stars with $5500 \text{ K} \geq T_{\text{eff}} \geq 5000 \text{ K}$ (probably RHB), and 2.0 km s^{-1} for stars with $T_{\text{eff}} < 5000 \text{ K}$ (RHB or RGB).

Input color temperatures T_{B-V} and T_{V-K} were computed from the B , V , K , and $E(B-V)$ values of Table 1, assuming $E(V-K) = 2.7E(B-V)$. However, we found literature reddening estimates for only 98 (28%) of our 340 program stars. Additionally, while 77 of these reddening values are adopted from Bailer-Jones (2011), the remaining 21 values come from various sources listed in Table 1. This constitutes a very heterogeneous set of reddening values, and they should be viewed with caution. In particular, we note that the reddening values for five program stars appear to be unreasonably large for their apparent magnitudes: HIP 34959 ($E(B-V) = 0.28$, $V = 7.87$), HIP 38852 (0.36, 8.75), HIP 48979 (0.15, 9.64), HIP 52817 (0.25, 8.69), and HIP54858 (0.29, 7.92). In these cases we neglected reddening corrections when computing input color temperatures. We used the color- T_{eff} relationships of Ramírez & Meléndez (2005) to compute $T_{\text{eff},B-V}$ and $T_{\text{eff},V-K}$, which are listed in Table 3. For a given star, if $|T_{\text{eff},B-V} - T_{\text{eff},V-K}| < 200 \text{ K}$ we used their mean as the color temperature $T_{\text{eff},color}$. If this difference was beyond 200 K we adopted $T_{\text{eff},color} = T_{\text{eff},V-K}$, as it is less sensitive to metallicity than is $T_{\text{eff},B-V}$.

As described in Böcek Topcu et al. (2015), we used the central depth ratios of up to 14 temperature-sensitive line pairs in the 6200 Å spectral range to provide $T_{\text{eff},LDR}$ estimates of our RHB candidates. The LDR method was developed initially by Gray & Johanson (1991), and expanded by several authors, most importantly for our work by Biazzo et al. (2007a,b). The attraction of the LDR method is that it is insensitive to interstellar reddening, and it is a direct spectrum measurement that is not dependent on a model atmospheric analysis. The $T_{\text{eff},LDR}$ values from our spectrum depth measurements and the Biazzo et al. (2007a) formulae are listed in Table 3.

For the final input $T_{\text{eff}\star}$ we again invoked an empirical rule that if $|T_{\text{eff},LDR} - T_{\text{eff},color}| < 200 \text{ K}$ we used the mean value of these two estimates, but if the difference was greater than 200 K we used $T_{\text{eff},LDR}$ only because of its freedom from interstellar reddening uncertainties.

Physical gravities can be calculated in a straightforward manner from:

$$\log g_{phy} = 0.4 (M_{V\star} + BC - M_{\text{Bol}\odot}) + \log g_{\odot} + 4 \log\left(\frac{T_{\text{eff}\star}}{T_{\text{eff}\odot}}\right) + \log\left(\frac{m_{\star}}{m_{\odot}}\right).$$

where $M_{\text{bol}} = 4.75$, $\log g = 4.44$, and $T_{\text{eff}} = 5777 \text{ K}$. The bolometric corrections (BC) were estimated using the numerical relations provided by Flower (1996).

The stellar quantities needed for this equation were not so easy to specify. First, we lacked information on the masses of our stars, so we arbitrarily assumed $m_{\star} = 1.0 m_{\odot}$. Second, our analyses were completed prior to the first Gaia data release, so M_V values were available only for about 70% of our program stars. For the rest, we assumed initial $\log g$ values of 3.7 for $T_{\text{eff}} > 5500 \text{ K}$ (likely subgiants), 2.3 for $T_{\text{eff}} < 5000 \text{ K}$ (likely red giants), and 3.0 for $5000 \text{ K} < T_{\text{eff}} < 5700 \text{ K}$ (candidate RHB stars). Finally, for T_{eff} we used the mean of the input color and LDR temperatures.

6.2. Final Parameters

The initial parameters, and those determined iteratively as described below, were used to create interpolated model atmospheres from the ATLAS grid (Kurucz 2011)⁷ using software developed by Andy McWilliam and Inese Ivans.

Our semi-automated code uses EW ’s of Fe I, Fe II, Ti I, and Ti II transitions to derive individual line abundances. The goal of the model iterations by the code was to determine the model T_{eff} , $\log g$, ξ_t , and $[M/H]$ that: (1) eliminates or minimizes slopes in the abundance $\log \epsilon$ versus excitation energy χ and versus reduced equivalent width RW ($\equiv \log(EW/\lambda)$); (2) forces agreement between derived $\log \epsilon$ values of the two species of Fe and Ti; and (3) yields

⁷ <http://kurucz.harvard.edu/grids.html>

derived metallicity $[M/H]$ in agreement with the assumed model metallicity. For each iteration on model parameters the abundance trends can be inspected in text and graphical form after code completion, so that a user can judge the quality of the final chosen model. Our use of this code followed those of [Böcek Topcu et al. \(2015, 2016\)](#) in all aspects. In particular, in deriving $\log g$ from the Fe and Ti ionization balances we assigned more weight to Fe (65%) than to Ti (35%). We have also investigated the effects of independent Fe and Ti ionization balances by varying the weight given to the Ti ionization balance 0 and 100 in the $\log g$ determinations. For this experiment, we selected 10 RHB candidates that are the good representatives of our entire sample: HIP 476, HIP 4197, HIP 8423, HIP 9557, HIP 10872, HIP 23949, HIP 74058, HIP 78990, HIP 94598 and HIP 106775. The derived $\log g$ values changed by only 0.2 dex on average, which is well within the uncertainties derived in §6.3.

The atomic line lists adopted in this work to compute the model atmospheric parameters and species relative abundances are those of [Böcek Topcu et al. \(2015, 2016\)](#); we briefly summarize them here. The spectral range was about 5200–7100 Å to avoid telluric line contamination at redder wavelengths and severe line crowding at bluer wavelengths. We formed lists of relatively unblended lines by using several solar atlases ([Moore et al. 1966](#), [Delbouille et al. 1973](#), [Kurucz et al. 1984](#), [Wallace et al. 2011](#)), the Arcturus spectral atlas ([Hinkle & Wallace 2005](#)), and the interactive database of high-resolution standard star spectra SpectroWeb⁸ ([Lobel 2008, 2011](#)). The model atmospheric parameters of our program RHBs were determined using a maximum of 70 Fe I, 12 Fe II, 11 Ti I and 6 Ti II lines; the numbers varied from star to star. We used EW limits for both neutral and ionized Fe and Ti lines defined by [Böcek Topcu et al.](#), discarding very weak and very strong lines to retain only those in the range $RW \simeq -5.8$ to -4.6 (equivalent to $EW \simeq 10$ mÅ to 150 mÅ at 6500 Å). We did not apply these limitations to the other species since they have fewer transitions. The transition probabilities were taken from single source laboratory-based homogeneous studies as much as possible. In particular, we used the University of Wisconsin atomic physics group lab data for Ti I ([Lawler et al. 2013](#)), Ti II ([Wood et al. 2013](#)), and Ni I ([Wood et al. 2014b](#)). Unfortunately the fundamental metallicity-defining element Fe has no single comprehensive lab study for either its neutral or ionized species. Therefore we adopted several sources that together should yield reliable species abundances. For Fe I, those are [O’Brian et al. \(1991\)](#) (lines with excitation energies $\chi < 2.1$ eV) and [Den Hartog et al. \(2014\)](#), [Ruffoni et al. \(2014\)](#) (lines with $\chi \geq 2.1$ eV). For Fe II (lacking any recent detailed lab work), we used gf -values from the NIST Atomic Spectra Database⁹. For gf values of remaining species Si I, Ca I, Cr I and Cr II we have used several sources, which are given in Table 4 of both [Böcek Topcu et al. \(2015\)](#) and [Böcek Topcu et al. \(2016\)](#).

In Figure 6 we compare the final spectroscopic temperatures $T_{\text{eff},sp}$ to the initial LDR and photometric estimates. In panel (a) the correlation with $T_{\text{eff},LDR}$ is linear with small scatter. For the 270 stars with $T_{\text{eff},sp} < 5200$ K, a simple mean offset is $\langle T_{\text{eff},LDR} - T_{\text{eff},sp} \rangle = 108 \pm 7$ ($\sigma = 124$). Above this temperature the $T_{\text{eff},LDR}$ values asymptotically approach 5300 K while the $T_{\text{eff},sp}$ ones continue to rise. The [Gray & Johanson \(1991\)](#) and [Biazzo et al. \(2007a\)](#) LDR formulae predominantly use the depths of low excitation V I lines as the numerators of their ratios. At the R and S/N of our spectra, these V I lines become very weak at warmer T_{eff} values and the T_{eff} formulae tend toward single values. ASF12 included the LDR ratios of [Strassmeier & Schordan \(2000\)](#), which used species other than V I, for stars with $T_{\text{eff},sp} \geq 5500$ K (see their Figure 3). However, the comparison between spectroscopic and LDR temperatures for the [Biazzo et al.](#) and [Strassmeier & Schordan](#) relations were offset by roughly 300 K. Since stars with $T_{\text{eff}} \gtrsim 5500$ K were not of prime interest to our RHB work, we have not pursued this issue further.

At the lower temperature and higher metallicity end of the sample, our chosen Fe and Ti lines have strengths large enough that all lie on the flat or damping parts of the curve-of-growth. For these stars, it is very difficult to determine independent values of T_{eff} and ξ_t . Therefore, for a few of these stars we adopted a fixed value of ξ_t between 1.2 and 1.6 km s⁻¹, and varied only T_{eff} , $\log g$, and $[Fe/H]$ during the model iterations. We also adopted fixed ξ_t values between 0.5 and 1.2 km s⁻¹ for about 30 stars with $\log g > 3.5$.

In panels (b) and (c) we compare spectroscopic temperatures with $(V - K)$ and $(B - V)$ photometric temperatures. Qualitatively the correlations show good agreement with reasonably small scatter for stars with $T_{\text{eff},sp} \lesssim 5200$ K, but significant scatter appears for warmer stars. The following cautions should be kept in mind here. The photometry is heterogeneous, taken from SIMBAD and ultimately based on a variety of original sources. The reddening estimates exist only for some of our RHB stars, and those reddening values have various uncertainties. Finally, as discussed in [Ramírez & Meléndez \(2005\)](#) $(B - V)$ photometric temperatures are more dependent on $\log g$ and metallicity than are $(V - K)$ temperatures. This creates more scatter among the $(B - V)$ temperatures, especially at temperatures

⁸ <http://alobel.freeshell.org/spectrowebl.html>

⁹ <https://www.nist.gov/pml/atomic-spectra-database>

$\gtrsim 5200$ K.

Thus it is not surprising that there are relatively weak correlations between spectroscopic and photometric temperatures.

In Figure 7 we compare the input gravities $\log g_{phys}$ computed with the above formula, and those derived from our spectroscopic analysis. On average the correlation is good, albeit with large star-to-star scatter: $\langle \log g_{phys} - \log g_{spec} \rangle = +0.05 \pm 0.03$ ($\sigma = 0.51$, 318 stars). Our physical gravity estimates depend linearly on assumed stellar masses, and in the figure we indicate how these gravities would change if the masses were doubled.

The complete set of derived model atmospheric parameters for our program stars are listed in Table 3. Using the final T_{eff} and $\log g$ values, we have constructed an HR diagram in spectroscopic units in Figure 8. The gray-shaded regions of this plot, $T_{\text{eff}} > 5500$ K, $T_{\text{eff}} < 4500$ K, and/or $\log g > 3.5$, represent the parameter space of program stars that are unlikely to contain true RHB members. The color range of our program stars inside the RHB domain defined by Kaempf et al. (2005) is $(B - V) \simeq 0.6 - 1.0$ (Figure 3). This color interval corresponds to a temperature range $T_{\text{eff}} \sim 4800 - 5800$ K, using the color-temperature calibrations of Ramírez & Meléndez (2005); see their Figure 3. Our sample has only seven stars with $5500 \text{ K} < T_{\text{eff}} < 5800 \text{ K}$ and $\log g < 3.5$; just one of these has $\log g < 3.0$. Proof of chemically-evolved status (Afşar et al. 2018) for these stars would be difficult because they will have generally very weak/absent molecular bands and [O I] lines. Therefore they are not included in the RHB domain as defined here. We do retain stars in the $4500 \text{ K} < T_{\text{eff}} < 4800 \text{ K}$ range for now, and will consider their RHB/RGB status in the next paper.

ASF12 defined RHB stars through a combination of position in the $T_{\text{eff}} - \log g$ plane and proof of internal CN-cycle H-fusion and mixing, as evidenced in low surface carbon isotopic ratios, $^{12}\text{C}/^{13}\text{C} < 30$. They did so because stars with masses $m \sim 2.5 - 4.5 m_{\odot}$ pass through the RHB domain during their SGB evolution, prior to their completion of the 1st dredge-up phase. A large majority of the ASF12 RHB candidates with temperatures between 4800 K and 5500 K proved to be mixed stars. Of the 45 stars in this T_{eff} range with $\log g < 3.5$, nine had $^{12}\text{C}/^{13}\text{C} \gtrsim 30$ or undetermined (20%); these stars had essentially undetectable ^{13}CN features in their spectra. The isotopic ratios derived for the remaining 36 stars (80%) showed clear evidence for internal evolution: 15 of them had $^{12}\text{C}/^{13}\text{C} = 20 - 29$, 14 had $^{12}\text{C}/^{13}\text{C} = 10 - 19$, and 7 had $^{12}\text{C}/^{13}\text{C} < 10$. Therefore we expect our program stars with in this (T_{eff} , $\log g$) domain of Figure 8 to be dominated by evolved stars. We adopt the unshaded region of Figure 8, $4500 \text{ K} \leq T_{\text{eff}} \leq 5500 \text{ K}$ and $\log g \leq 3.5$, as the ‘‘RHB domain’’. This is a generous definition, and includes stars with $\log g$ values between 3.0 and 3.5 that may well turn out to be subgiants, and stars with $T_{\text{eff}} \lesssim 4800$ K that may be an admixture of RC and RGB stars. More definitive RHB membership statements about individual stars will require the CNO analysis in Afşar et al. (2018).

6.3. Parameter Uncertainties and Comparison with Previous Studies

To investigate the internal uncertainties in atmospheric parameters, we selected two stars that are good representatives of our entire sample; HIP 4197 and HIP 10872. We ran a series of analyses by varying the stellar atmospheric parameters in steps of 50 K for T_{eff} , 0.05 dex for $\log g$ and 0.05 km s^{-1} for ξ_t on the spectral data of both stars. Individual uncertainties were estimated by varying one parameter at a time while others were fixed during the each analysis. To determine the uncertainty in T_{eff} we searched for the temperature excursion that creates a $\pm 1\sigma$ scatter in the abundance difference between low- and high-excitation Fe I lines. Applying this method resulted in estimated T_{eff} uncertainties of ~ 150 K for both stars. The same method was applied to determine the uncertainties in $\log g$ and ξ_t . The typical average uncertainties in these parameters were found to be ~ 0.25 dex and $\sim 0.25 \text{ km s}^{-1}$, respectively. We have also investigated the effects of atmospheric parameter uncertainties on the elemental abundances of both HIP 4197 and HIP 10872 and listed the mean sensitivities in Table 4. The results indicate that effective temperature uncertainties contribute most to the abundance uncertainties of neutral species, while surface gravity uncertainties mainly affect those of the ionized species. However, this means that the sensitivities of abundance ratios $[X/\text{Fe}]$ are not large (see §7.2).

External (scale) uncertainties can be estimated by comparing our results with the previous studies that have stars in common with our sample. First we comment on the parameters newly determined in this study for the stars previously published in ASF12. There are 45 such stars, counting the few with double analyses here as separate objects. Forming mean differences for an atmospheric quantity X in the sense $\langle \Delta X \rangle = \langle X_{ASF12} - X_{new} \rangle$, we find $\langle \Delta T_{\text{eff}} \rangle = +23 \pm 12$ K ($\sigma = 87$ K), $\langle \Delta \log g \rangle = +0.17 \pm 0.04$ ($\sigma = 0.30$), $\langle \Delta \xi_t \rangle = -0.07 \pm 0.02$ ($\sigma = 0.16$), and $\langle \Delta [\text{Fe}/\text{H}] \rangle = +0.03 \pm 0.02$ ($\sigma = 0.11$). In ASF12 we made use of only neutral and ionized species of Fe for model atmosphere analysis, while the present work takes two species of Fe and Ti into account for the analysis. The effect of updated gf -values on model atmosphere calculations should also be considered when assessing the difference between the old and newly determined

parameters. Our new analyses are in good accord with those of ASF12.

The largest compilation of stellar parameters relevant to our work is the PASTEL catalog (Soubiran et al. 2016). There are many more entries in this catalog for MS, SGB, and RGB stars than for the comparatively rare RHB stars. A non-exhaustive search through this database found 225 entries for 88 of our program stars. Here we opted to treat multiple PASTEL entries from different literature sources for individual stars as separate entities. In Figure 9 we correlate that catalog’s T_{eff} , $\log g$, and $[\text{Fe}/\text{H}]$ values with those determined in this work. Taking differences in the sense PASTEL entry *minus* this study, we find good agreement for effective temperature and metallicity: $\langle \Delta T_{\text{eff}} \rangle = +45 \pm 7 \text{ K}$ ($\sigma = 102 \text{ K}$), and $\langle \Delta [\text{Fe}/\text{H}] \rangle = +0.03 \pm 0.01$ ($\sigma = 0.12$). Our gravities are typically smaller than those from the literature: $\langle \Delta \log g \rangle = +0.29 \pm 0.02$ ($\sigma = 0.34$), but the star-to-star scatter clearly is large. The uncertainty in gravity does not appear to affect the metallicity comparison, and our $\log g$ values are on an internally-consistent system, whereas the PASTEL entries reflect the results of scattered literature sources.

Luck (2015) (and references therein) reported model atmosphere parameters and abundances for 1133 F, G, and K ($3800 \text{ K} \gtrsim T_{\text{eff}} \gtrsim 7800 \text{ K}$) luminosity class III stars. We have 48 stars in common with their more general evolved star survey. Figure 10 panels (a)-(c) illustrate the excellent agreement between our derived values of T_{eff} , $\log g$, $[\text{Fe}/\text{H}]$ and theirs. Defining differences in the sense $\Delta X \equiv X_{\text{luck15}} - X_{\text{this study}}$, we find: $\Delta T_{\text{eff}} = +15 \pm 13 \text{ K}$ ($\sigma = 88 \text{ K}$); $\Delta \log g = +0.01 \pm 0.03$ ($\sigma = 0.24$); and $\Delta [\text{Fe}/\text{H}] = +0.04 \pm 0.01$ ($\sigma = 0.09$). The mean values and scatters are entirely within the uncertainties in these quantities in the two studies. We will comment on the $[\alpha/\text{Fe}]$ values of Figure 10 panel (d) below.

7. DERIVED ABUNDANCES

7.1. Metallicities

Our program stars span the derived metallicity range $-2.0 \lesssim [\text{Fe}/\text{H}] \lesssim +0.4$, but only two stars have $[\text{Fe}/\text{H}] < -1.5$: HIP 38852 ($[\text{Fe}/\text{H}] = -2.05$) and HIP 79518 (-1.89). Although we have a large stellar sample, our target selection was accomplished primarily with temperature and luminosity criteria; no attempt was made to achieve statistical completeness of the disk metallicity domain. For program stars with measured parallaxes (Table 2), only 12 lie at distances greater than 1000 pc. Although some of the 31 stars without parallax data may be at large distances, at most this is about a 10% effect; our stellar sample is relatively local. Thus major statements about overall Galactic disk populations are not warranted. With that caution in mind, a few general conclusions can be drawn about the metallicity distribution function of our sample.

In Figure 11 we show metallicity histograms of our stars with $[\text{Fe}/\text{H}] \geq -1.5$, excluding the two low-metallicity stars which are of less interest here. In panel (a) histograms are displayed for all stars and for just the ones in the RHB domain as defined in §6 and depicted in Figure 8. These two histograms are very similar, thus are sampling the same Galactic disk metallicity distribution function. There is a significant tail of stars with $[\text{Fe}/\text{H}] \lesssim -0.5$, indicating the presence of a substantial thick disk component to our sample. In this panel we mark the locations of the median and mean values, $[\text{Fe}/\text{H}] = -0.20$ and -0.28 , respectively. These are significantly offset from the solar metallicity.

Our field RHB metallicity distribution appears to be consistent with those of some other spectroscopic Galactic disk surveys. Here we consider two examples. Bensby et al. (2014) conducted an abundance study of 714 F- and G-type dwarf and subgiant stars that were kinematically chosen to represent disk and halo components of the Galaxy. Inspection of their Figure 2 suggests that the metallicity distribution of their stars in kinematic thin disk, thick disk, and halo bins do not resemble that of our program stars. However, selecting the Bensby et al. stars with thick disk to thin disk kinematic probability ratios $TD/D < 2$ (the stars of panels (c) and (d) of their Figure 2) produces the metallicity distribution shown in panel (b) of Figure 11. This distribution is broadly similar to ours. A systematic shift in our metallicity scale by $+0.1$ dex would produce essential agreement between the peaks of two distributions for stars with $[\text{Fe}/\text{H}] \gtrsim -0.2$ dex, but the metallicity widths are clearly a bit different – our distribution in $[\text{Fe}/\text{H}]$ appears to be narrower than that of Bensby et al.

The APOGEE near-IR spectroscopic survey (Holtzman et al. 2015; Majewski et al. 2016) is much more statistically robust, and inspection of Table 2 and Figure 5 of Hayden et al. (2015) suggests that our average and peak metallicities correspond to stars with Galactocentric radius $R \sim 10\text{--}11$ kpc for heights above the Galactic plane inside $|z| < 0.5$ kpc, and $R \sim 6\text{--}10$ kpc for $0.5 < |z| < 1.0$ kpc. These distance parameters cover a Galactic volume not very much different than that containing our program stars. Given the lack of cross-calibration between our metallicity scale and that of APOGEE, the concordance is reasonable.

7.2. Abundance Ratios

In this paper we report abundances for the α elements Si and Ca, the α -like element Ti¹⁰ and Fe-group elements Cr and Ni. Both neutral and ionized species have been investigated for Ti and Cr.

Abundance ratios $[X/Fe]$ for all program stars are listed in Table 5 and plotted as functions of $[Fe/H]$ metallicities in Figure 12. These ratios have been formed from same-species abundances, that is $[X \text{ I}/Fe \text{ I}]$ and $[X \text{ II}/Fe \text{ II}]$. Therefore, as mentioned in §6.3, the sensitivities of these ratios to the uncertainties in atmospheric parameters are much smaller than the absolute uncertainties in the individual species abundances.

For comparison with our results, we also have plotted the metallicities and abundance ratios of three large-sample surveys of Galactic disk main sequence and early subgiant field stars published by Reddy et al. (2003, 2006) and Bensby et al. (2014).

In general the abundance ratios of our program stars follow the trends with metallicity established by these higher-gravity field stars. From Figure 12 we note that:

1. α elements of left-hand panels (a)–(d) show the familiar increase in relative abundance ratios with decreasing $[Fe/H]$ metallicity, reaching $[X/Fe] \simeq +0.25$ with ± 0.15 scatter.
2. The two species of Ti are in reasonable accord as expected from their roles in assisting with our $\log g$ determinations; $\langle Ti \text{ II} - Ti \text{ I} \rangle = +0.06$ ($\sigma = 0.06$).
3. Si exhibits much star-to-star scatter (panel a). We repeated the analysis for a few stars that show considerable scattering in Si abundance. A common feature in six of these stars with $[Fe/H] \gtrsim 0$ and $[Si/Fe] \sim 0.35$ dex is that the lines used for the model atmosphere analysis have a very narrow RW range that requires a fixed microturbulent velocity for the solution. Therefore, these results should be interpreted with caution. A further concern is the effective temperature dependence of Si. As seen in Figure 13, $[Si/Fe]$ increases as the T_{eff} decreases. Investigation of the metallicity dependency of this relation showed no obvious connection to the metallicity, in other words, whatever the metallicity is, the relative Si abundance seems to increase depending on effective temperature.¹¹ Underlying causes of this behavior need further investigation.
4. The two Cr species have a mean abundance offset (panels e, f): $\langle Cr \text{ II} - Cr \text{ I} \rangle = +0.05$. However, many Cr II abundances are anomalously large, leading to $\sigma = 0.31$, a scatter that overwhelms the mean offset. For Cr II we have only five transitions (4588.20, 4592.05, 5237.32, 5305.87 and 5334.86). Our adopted transition probabilities from Böcek Topcu et al. (2015) have recently been revised by Lawler et al. (2017). For our lines the scatter old-new in $\log gf$ values is high but the mean is essentially the same. The 4588 and 4592 lines are in a crowded spectral region; blending with other transition(s) may be of concern. For most of the RHBs there are only one or two Cr II lines to be trusted for the abundance. Moreover, in Table 5 there are RHBs whose Cr II abundances are based on only one line. For all of these reason the overall star-to-star scatter in Cr II abundances is higher than in Cr I; caution is warranted in interpreting panel (f) of Figure 12.

Further insight is gained by forming mean abundances of the Fe group and α elements. In panel (a) of Figure 14 we show the mean $[X/Fe]$ values of the three Fe-group species. The trend with metallicity is nearly flat, with little star-to-star variation. Defining $[Fe \text{ group}/Fe] = \langle [Cr \text{ I}/Fe], [Cr \text{ II}/Fe], [Ni \text{ I}/Fe] \rangle$, for the whole sample, $\langle [Fe \text{ group}/Fe] \rangle = 0.00$ with $\sigma = 0.05$. These values are, as expected, consistent with solar Fe group abundance ratios and star-to-star scatter dominated by observational/analytical uncertainties.

In panel (b) of Figure 14 we plot $[\alpha/Fe]$ (the simple mean of $[Si \text{ I}/Fe]$, $[Ca \text{ I}/Fe]$, $[Ti \text{ I}/Fe]$, $[Ti \text{ II}/Fe]$) versus $[Fe/H]$. A pale red line has been drawn at $[\alpha/Fe] = +0.13$ with a width $\delta[\alpha/Fe] = 0.04$. This line is a reasonable estimate of the division between α -solar and α -rich stars in our sample. This separation has been suggested by several authors and has been studied extensively in the very large APOGEE survey (e.g., Martig et al. 2015 and references therein). In our sample the α -rich group occurs at lower metallicities, $[Fe/H] \lesssim -0.3$ and has an average $[\alpha/Fe] \simeq +0.25$. The growth in $[\alpha/Fe]$ with decreasing $[Fe/H]$ reaches a plateau at $[Fe/H] \simeq -0.5$, in accord with so-called the “knee” defined in previous studies (e.g., Bensby et al. 2003; Reddy et al. 2006; Liu & van de Ven 2012; Bensby et al. 2017). At lower metallicities $\langle [\alpha/Fe] \rangle$ remains nearly constant, and at higher metallicities it declines to about +0.05. The average metallicity of the group with solar $[\alpha/Fe]$ values occurs at about $[Fe/H] \simeq -0.1$. This is all in accord with previous

¹⁰ True α elements are those whose major naturally-occurring isotopes are composed of multiples of ^4He nuclei; these include the observable elements Mg, Si, S, and Ca. The Ti abundance is dominated by ^{48}Ti (73% in the solar system), and the α from ^{44}Ti is unstable with a short half-life. Since the $[Ti/Fe]$ ratio exhibits the same general trend with metallicity as does the real α elements, it often is given the same element group name.

¹¹ A similar effect for very metal-poor stars has been found in Si abundances derived from the Si I 3905 Å line (not employed here); see, e.g., Sneden & Lawler (2008), and references therein

results from low luminosity main sequence and subgiant stars (e.g., Reddy et al. 2006; Anders et al. 2014; Martig et al. 2015; Bensby et al. 2017). Additionally, all but one of our 48 program stars also investigated by Luck (2015) (see §6.3) fall into the metallicity range $[\text{Fe}/\text{H}] \gtrsim -0.7$ (the lone exception has $[\text{Fe}/\text{H}] = -1.43$). Inspection of panel (d) of Figure 10 shows that the agreement in $[\alpha/\text{Fe}]$ between the two studies is excellent: $\Delta[\alpha/\text{Fe}] = +0.01 \pm 0.00$ ($\sigma = 0.03$).

8. CORRELATIONS BETWEEN KINEMATICS AND CHEMICAL COMPOSITIONS

Understanding the relation between chemical compositions and kinematics of stars is essential to better constrain Galactic evolutionary scenarios. In Figure 15, we present a version of Figure 14(b) with the symbols coded in thin disk, thick disk, and halo velocity groups defined as in Figures 4 and 5. The lower metallicity α -rich group ($[\alpha/\text{Fe}] > +0.13$) is dominated by thick disk stars. The very high velocity stars presumed to be members of the Galactic halo have $[\alpha/\text{Fe}]$ ratios generally consistent with those of α -rich thick disk stars. Higher metallicity α -solar group has nearly all of the thin disk stars, but also has a significant amount of thick disk stars with nearly circular orbits (see §9). Since the chemical separation seems more discernible than kinematic separation, here we prefer to use the term “chemically thin disk (α -solar) / chemically thick disk (α -rich)”.

In Figure 16, we plot the UVW velocity components as functions of $[\text{Fe}/\text{H}]$ and $[\alpha/\text{Fe}]$. At a metallicity of $[\text{Fe}/\text{H}] \lesssim -0.3$, all velocity components begin to substantially increase their dispersions, as discussed in, e.g., Edvardsson et al. (1993), Reddy et al. (2006), Bensby et al. (2011) and Anders et al. (2014). In $[\alpha/\text{Fe}]$, this velocity-dispersion increase appears at about $+0.13$ dex. Of the three velocity components, W_{LSR} component shows this transition most distinctly in both $[\text{Fe}/\text{H}]$ and $[\alpha/\text{Fe}]$ (panels (c) and (f), respectively). Specifically, the transition is from a dispersion of about $|W_{\text{LSR}}| \simeq 40 \text{ km s}^{-1}$ at $[\alpha/\text{Fe}] \simeq +0.13$ to 80 km s^{-1} at $[\alpha/\text{Fe}] > +0.13$. This sharp change in the velocity dispersion represents the transition between the kinematically cold thin disk to the kinematically hotter thick disk, and has been seen before, e.g., in Reddy et al. (2006) and Brook et al. (2012).

9. ORBITAL CHARACTERISTICS AND CHEMICAL COMPOSITIONS

In Figure 17 we investigate the distribution of metallicities, relative α abundances, and W_{LSR} velocity components as functions of Galactic orbital eccentricities, e . As seen in panel (a), $[\text{Fe}/\text{H}]$ has a strong trend with eccentricity kinematically thick disk stars, for those with $e > 0.25$, as previously discussed by, e.g., Lee et al. (2011) and Boeche et al. (2013). The $[\alpha/\text{Fe}]$ ratios also correlate with eccentricity (panel (b) of the figure) but there is less distinct grouping – a number of thin disk stars are α -rich and many thick disk stars are α -solar ($[\alpha/\text{Fe}] \lesssim +0.13$, $W_{\text{LSR}} \lesssim 40 \text{ km s}^{-1}$). Finally, the dispersion in W_{LSR} space velocities clearly is larger for the thick disk and halo stars than those of the thin disk (panel (c) of the figure). In short, these three observable aspects of stars in our RHB sample all correlate with derived orbital eccentricities, and yield a set of stellar population characteristics that is consistent with that determined from main sequence stars in previous surveys (as cited above, particularly in §7.2).

Further insight can be gained from correlations between eccentricity, $[\text{Fe}/\text{H}]$ and $[\alpha/\text{Fe}]$ with Galactocentric distance, as displayed in Figure 18. We define a mean Galactocentric distance as $R_{\text{m}} = (R_{\text{pericenter}} + R_{\text{apocenter}})/2$. The low eccentricity, α -solar, high metallicity stars are mostly located within the solar radius zone ($7 \text{ kpc} < R_{\text{m}} < 9 \text{ kpc}$). However, our RHB stars with thick disk and halo eccentricities (panel (a) of the figure) generally lie at radii smaller than that of the solar circle; most have $5 \text{ kpc} < R_{\text{m}} < 7 \text{ kpc}$. The separation in R_{m} becomes more distinct if the higher-metallicity, lower $[\alpha/\text{Fe}]$ stars are grouped with the thin disk members. The overwhelming number of thick disk RHB stars with $[\alpha/\text{Fe}] \gtrsim +0.2$, and $[\text{Fe}/\text{H}] \lesssim -0.3$ have relatively small R_{m} values.

Although our sample along R_{m} is not complete, it still resembles the findings presented by, e.g., Edvardsson et al. (1993), Anders et al. (2014) and Hayden et al. (2015), where they discuss the $[\alpha/\text{Fe}]$ – $[\text{Fe}/\text{H}]$ relation over a large Galactocentric distance. In all cases, two distinct α -groups appear with a mean $[\alpha/\text{Fe}] \simeq 0.25$ dex for the inner-group ($R_{\text{m}} < 7 \text{ kpc}$) stars. The mean α abundance is $\langle[\alpha/\text{Fe}]\rangle \simeq 0.1$ dex for the outer-group ($R_{\text{m}} > 8.0 \text{ kpc}$) stars. In our sample, inner-stars are mostly composed of kinematically thick disk stars, as discussed above, while the outer-group contains all kinematic classes. Interestingly, four of the nine stars kinematically classified as halo members are located the closest to the Galactic center in our entire sample. Their $[\alpha/\text{Fe}]$ values are all high (around 0.3), while their $[\text{Fe}/\text{H}]$ metallicities vary substantially.

With Figure 19, we investigate the total orbital energy (E_{tot}) and the orbital angular momentum (L_z), i.e., the integrals of motion in an axisymmetric potential. In panel (a) of the figure we plot the E_{tot} as a function of the L_z . Grey triangles represent α -rich ($[\alpha/\text{Fe}] > +0.13$) stars, while red dots represent the α -solar stars in our sample.

α -solar stars occupy the domain of rotationally supported orbits, predominantly the thin disk.¹² The α -rich stars occupy the whole kinematic domain, from the thin/thick disk to halo. Among these stars, the most energetic ones are on retrograde orbits.

However, most of the α -rich stars have lower E_{tot} with less L_z , indicating that they mostly spend their time in the inner regions of the Galaxy and have less disk-like rotation than the α -solar stars. This result is in accord with our conclusions from the velocity analysis. We also note a tight group of five stars in this plot. They have nearly zero angular momentum and very low orbital energy, practically the lowest in our sample; we will further investigate these below. In Figure 19 panels (b) and (c), we show the orbital eccentricity, e , as a function of E_{tot} and L_z , respectively (Galactic orbital parameters are listed in Table 6). α -solar stars have moderate energies with mostly disk-like and nearly circular ($e < 0.3$) orbits, though there are a few exceptions. The most notable is the star with the highest eccentricity, $e \simeq 0.8$; this is the same star discussed above, which is on a retrograde orbit (see also panels (a) and (c)), and likely is an accreted star. α -rich stars show all the range of eccentricities. Two high-velocity α -rich stars that appear on retrograde orbits (panel (c)) draw attention with their thick-disk-like eccentricities. The most energetic stars are also highly eccentric; however, the lowest energy ones are also highly eccentric. These latter ones are the same group of five stars noted before, with nearly zero angular momentum (panels (a) and (c)). They are practically on radial orbits, and spending their time in the inner regions of the Galaxy. Their $[\alpha/\text{Fe}]$ ratios range from +0.23 to +0.30 with an average of +0.28 dex ($\sigma = 0.03$) while $[\text{Fe}/\text{H}]$ varies from -2.05 to -0.49 . Their Ni and Cr abundances are nearly solar. The $[\text{Fe}/\text{H}]$ and $[\alpha/\text{Fe}]$ ranges of these halo stars with high-eccentricities and low-energies quite similar to the stars presented in, e.g., Geisler et al. 2007, in which they discuss the Galactic halo formation (see their Figure 12). We will further investigate the profile of $[\alpha/\text{Fe}] - [\text{Fe}/\text{H}]$ relation for these stars, together with other element abundances in our future work Afşar et al. (2018).

10. SUMMARY AND DISCUSSION

We have conducted a high-resolution spectroscopic survey of 340 field red horizontal branch candidates. In this first paper on survey results we have focused on the chemo-kinematics of targets, deriving abundances from only those α and Fe-group element transitions that can be easily analyzed from EW measurements.

We selected the RHB candidates mainly using color temperature, luminosity, and surface gravity estimates; no kinematical criteria were applied. This selection was done several years before Gaia’s first data release. Therefore our RHB absolute magnitude values included some rough estimates, especially for the stars without Hipparcos parallax information. With new Gaia data we were able to obtain more accurate parallaxes for more program stars. These showed general consistency with Hipparcos values for $\pi_{\text{Hip}} > 0.03$ mas (Figure 2). Out of 340 program stars, 309 have Gaia and/or Hipparcos values, making it possible to construct a reliable CMD for more than 90% of the RHB candidates (Figure 3). With the Kaempf et al. (2005) definition of the RHB CMD domain we were able to separate the RHBs from the subgiants and main sequence stars in our sample.

Spectra of high-resolution ($R \simeq 60,000$) and high S/N (usually ≥ 150) were obtained with the echelle spectrographs of the McDonald Observatory 2.7m HJS and 9.2m HET telescopes. We also reanalyzed the spectra of 45 RHB stars studied by ASF12 in order to ensure internally consistent results among the whole RHB sample. From these spectra we determined the atmospheric parameters (T_{eff} , $\log g$, ξ_t , $[\text{Fe}/\text{H}]$) and $[\text{X}/\text{Fe}]$ abundance ratios for species Fe I, Fe II, Ti I, Ti II, Cr I, Cr II, Si I, Ca I, and Ni I. These analyses yielded 250 stars with $4500 < T_{\text{eff}} < 5500$ and $\log g < 3.5$ (Figure 8). Taking into account the estimated temperature and $\log g$ limits for RHB stars suggested by ASF12 we constrained the region of *true RHB candidates* (tRHBc) in both the $(B - V) - M_V$ and $T_{\text{eff}} - \log g$ planes. This confinement yielded in the end about 150 tRHBc.

We calculated space velocity components (U_{LSR} , V_{LSR} , W_{LSR}) for 305 stars (see §5) using the distances and proper motions from Gaia or Hipparcos, and RVs derived from our spectra (§3). From the Toomre diagram (Figure 5), we have concluded that our sample is made up of 215 thin disk, 80 thick disk and 10 halo stars. About 80% of the tRHBc appears in kinematical thin disk, while the rest are thick disk members.

Our kinematically unbiased sample has representation over a wide metallicity range, $-2.0 \lesssim [\text{Fe}/\text{H}] \lesssim +0.4$ (Table 3), but the majority of the stars have near-solar metallicities ($([\text{Fe}/\text{H}]) \sim -0.2$, $\sigma \sim 0.3$). We have only a few halo stars with $[\text{Fe}/\text{H}] < -1.0$. General metallicity and $[\alpha/\text{Fe}]$ ratio distributions (Figure 14b) of our disk stars are broadly similar to other studies that investigate larger, more statistically robust samples, such as, Liu & van de Ven (2012), Bensby et al. (2014), Anders et al. (2014), Luck (2015) and Hayden et al. (2015). Even with our relatively small sample

¹² The lone exception is a star that is on a retrograde orbit of relatively low energy. With an $[\text{Fe}/\text{H}] = -0.6$, this high-velocity star is likely accreted from a satellite similar to the present-day dwarf spheroidal (dSph) galaxies orbiting the Milky Way. This star fits the dSph $[\alpha/\text{Fe}]$ versus $[\text{Fe}/\text{H}]$ pattern (e.g., Geisler et al. 2007), more specifically a Sagittarius dwarf-like system.

size we can see the bimodality in $[\alpha/\text{Fe}]$ at low metallicities and its extension towards $[\text{Fe}/\text{H}] \simeq -0.6$ discussed by, e.g., Nidever et al. 2014; Bensby et al. 2014, and references cited in those studies. The “knee” at $[\text{Fe}/\text{H}] \simeq -0.5$ (Bensby et al. 2003; Reddy et al. 2006; Bensby et al. 2017) also clearly appears in our sample. On the other hand, the Fe-group elements Cr and Ni have less variation with metallicity (Figure 14a); their abundance ratios are solar in all $[\text{Fe}/\text{H}]$ regimes of this study, in agreement with, e.g., Reddy et al. 2006; Bensby et al. 2014. Additionally, the chemically thin- and thick disk stars are on average kinematically separated: the high- α stars have larger space velocities, as seen in Figure 15.

Investigation of α abundances as functions of mean Galactocentric distances (Figure 18) indicated that the α -rich group resides mostly at $R_m < 7$ kpc, while α -solar stars mostly occupy the solar radius and some at $R_m > 9$ kpc. The α -solar group ($[\text{Fe}/\text{H}] > -0.3$, $[\alpha/\text{Fe}] \lesssim +0.13$) is mostly composed of kinematically thin disk stars. It also includes a number of thick disk stars with thin disk chemical compositions. The common feature of these stars that they have orbital eccentricities $e < 0.3$ (Figure 17) and they are mostly within the solar circle ($7 \text{ kpc} < R_m < 9 \text{ kpc}$, Figure 18), compared to their high eccentric counterparts. These α -solar stars have $|W_{\text{LSR}}| \lesssim 40 \text{ km s}^{-1}$, which indicates that they are kinematically located at smaller vertical scale heights and contribute mostly to the disk-like rotation. Regardless of their kinematic definitions, the stars around the solar neighbourhood may share a similar formation history that involves a metallicity enriched ISM via SNe Ia. Alternatively, as discussed in many studies (e.g., Sellwood & Binney 2002; Roškar et al. 2008; Haywood 2008; Schönrich & Binney 2009; Loebman et al. 2011; Lee et al. 2011; Boeche et al. 2013; Hayden et al. 2015; Daniel & Wyse 2015; Kordopatis et al. 2015, and references therein), old thick disk stars that were originally formed from enriched gas far from the solar neighborhood towards the Galactic center may appear in the solar radius due to radial migration of stars. Having a significant amount of kinematically thick disk stars at α -solar group may be also explained via radial migration of group of stars with originally thin disk kinematics now appearing at locations vertically more distant to the Galactic plane.

The $E_{\text{tot}} - L_z$ plot in Figure 19a shows that a few α -rich stars and one α -solar star are in retrograde orbits. There are five α -rich stars that appear clumped in the phase space (i.e., with near zero L_z , low orbital energy and high eccentricity). Their Galactocentric radii $R_m \sim 4.3$ kpc indicate that they spend most of their time in the inner regions of the Galaxy. Most of our sample is clustered at high L_z values, which increase with E_{tot} in disk-like rotations. α -solar stars have circular/near-circular orbits ($e < 0.3$) (Figure 19a), while α -rich stars have more eccentric orbits with less angular momenta implying less disk-like rotation. The α -rich stars that have similar energies, angular momenta and eccentricities to those of α -solar stars have mostly disk-like rotation and correspond to the high-metallicity tail of the kinematically thick disk stars.

The chemo-kinematical analysis of more than 300 RHB candidates allowed us to define the tRHBC in our sample. We identified about 150 tRHBC according to their HR diagram locations based on both $(B - V) - M_V$ and $T_{\text{eff}} - \log g$ criteria. The majority of them are kinematically thin disk members, while some has the kinematical thick disk membership. The second paper (Afşar et al. 2018) of this series will focus on the detailed chemical abundance analysis of these tRHBC. We will investigate CNO abundances and $^{12}\text{C}/^{13}\text{C}$ ratios along with many other elements such as α element Mg to complement Ca and Si reported in this paper; Fe-group elements: Sc, V, Mn, Co, Cu, Zn; and neutron-capture elements: Y, La, Nd, Eu. With the CNO abundances and $^{12}\text{C}/^{13}\text{C}$ ratios we will be able to investigate the evolutionary stages in detail and have more robust analysis to identify the tRHBC in our sample, and deepen the chemo-kinematic analysis we obtained in this study.

We thank Tim Beers, Earle Luck, and our referee for helpful discussions and comments on the manuscript. Our work has been supported by The Scientific and Technological Research Council of Turkey (TÜBİTAK, project No. 112T929), by the US National Science Foundation grants AST 1211585 and AST 1616040, and by the University of Texas Rex G. Baker, Jr. Centennial Research Endowment. This research has made use of the SIMBAD database, operated at CDS, Strasbourg, France. This work has made use of data from the European Space Agency (ESA) mission *Gaia* (<https://www.cosmos.esa.int/gaia>), processed by the *Gaia* Data Processing and Analysis Consortium (DPAC, <https://www.cosmos.esa.int/web/gaia/dpac/consortium>). Funding for the DPAC has been provided by national institutions, in particular the institutions participating in the *Gaia* Multilateral Agreement.

Software: IRAF (Tody 1993 and references therein), MOOG (Snedden 1973), ATLAS (Kurucz 2011)

REFERENCES

- Afşar, M., Böcek Topcu, G., Bozkurt, Z., & Sneden, C. 2018, *in preparation*.
 Afşar, M., Sneden, C., & For, B.-Q. 2012, *AJ*, 144, 20

- Alves, D. R., Rejkuba, M., Minniti, D., & Cook, K. H. 2002, *ApJL*, 573, L51
- Anders, F., Chiappini, C., Santiago, B. X., et al. 2014, *A&A*, 564, A115
- Bailer-Jones, C. A. L. 2011, *MNRAS*, 411, 435
- Behr, B. B. 2003, *ApJS*, 149, 101
- Bensby, T., Alves-Brito, A., Oey, M. S., Yong, D., & Meléndez, J. 2011, *ApJL*, 735, L46
- Bensby, T., Feltzing, S., & Lundström, I. 2003, *A&A*, 410, 527
- Bensby, T., Feltzing, S., & Oey, M. S. 2014, *A&A*, 562, A71
- Bensby, T., Feltzing, S., Gould, A., et al. 2017, *ArXiv e-prints*, arXiv:1702.02971
- Berdyugina, S. V., & Savanov, I. S. 1994, *Astronomy Letters*, 20, 755
- Biazzo, K., Frasca, A., Catalano, S., & Marilli, E. 2007a, *Astronomische Nachrichten*, 328, 938
- Biazzo, K., Pasquini, L., Girardi, L., et al. 2007b, *A&A*, 475, 981
- Böcek Topcu, G., Afşar, M., Schaeuble, M., & Sneden, C. 2015, *MNRAS*, 446, 3562
- Böcek Topcu, G., Afşar, M., & Sneden, C. 2016, *MNRAS*, 463, 580
- Boeche, C., Chiappini, C., Minchev, I., et al. 2013, *A&A*, 553, A19
- Brook, C. B., Stinson, G. S., Gibson, B. K., et al. 2012, *MNRAS*, 426, 690
- Brugamyer, E., Dodson-Robinson, S. E., Cochran, W. D., & Sneden, C. 2011, *ApJ*, 738, 97
- Casetti-Dinescu, D. I., & Girard, T. M. 2016, *MNRAS*, 461, 271
- Chen, Y. Q., Zhao, G., Carrell, K., & Zhao, J. K. 2011, *AJ*, 142, 184
- Chen, Y. Q., Zhao, G., Zhao, J. K., Xue, X. X., & Schuster, W. J. 2010, *AJ*, 140, 500
- Cruzalèbes, P., Jorissen, A., Rabbia, Y., et al. 2013, *MNRAS*, 434, 437
- Cutri, R. M., Skrutskie, M. F., van Dyk, S., et al. 2003, *2MASS All Sky Catalog of point sources*.
- Daniel, K. J., & Wyse, R. F. G. 2015, *MNRAS*, 447, 3576
- Dehnen, W., & Binney, J. 1998, *MNRAS*, 294, 429
- Delbouille, L., Roland, G., & Neven, L. 1973, *Atlas photometrique du spectre solaire de $[\lambda] 3000$ a $[\lambda] 10000$ (Liege: Universite de Liege, Institut d'Astrophysique)*
- Den Hartog, E. A., Ruffoni, M. P., Lawler, J. E., et al. 2014, *ApJS*, 215, 23
- Dinescu, D. I., Girard, T. M., & van Altena, W. F. 1999, *AJ*, 117, 1792
- Edvardsson, B., Andersen, J., Gustafsson, B., et al. 1993, *A&A*, 275, 101
- Fitzpatrick, M. J. 1993, in *Astronomical Society of the Pacific Conference Series*, Vol. 52, *Astronomical Data Analysis Software and Systems II*, ed. R. J. Hanisch, R. J. V. Brissenden, & J. Barnes, 472
- Flower, P. J. 1996, *ApJ*, 469, 355
- Gaia Collaboration, Brown, A. G. A., Vallenari, A., et al. 2016a, *A&A*, 595, A2
- Gaia Collaboration, Prusti, T., de Bruijne, J. H. J., et al. 2016b, *A&A*, 595, A1
- Geisler, D., Wallerstein, G., Smith, V. V., & Casetti-Dinescu, D. I. 2007, *PASP*, 119, 939
- Gilmore, G., & Reid, N. 1983, *MNRAS*, 202, 1025
- Goswami, A., & Karinkuzhi, D. 2013, *A&A*, 549, A68
- Gray, D. F., & Johanson, H. L. 1991, *PASP*, 103, 439
- Hawkins, K., Leistedt, B., Bovy, J., & Hogg, D. W. 2017, *MNRAS*, 471, 722
- Hayden, M. R., Bovy, J., Holtzman, J. A., et al. 2015, *ApJ*, 808, 132
- Haywood, M. 2008, *MNRAS*, 388, 1175
- Hesser, J. E., Harris, W. E., Vandenberg, D. A., et al. 1987, *PASP*, 99, 739
- Hinkle, K., & Wallace, L. 2005, in *Astronomical Society of the Pacific Conference Series*, Vol. 336, *Cosmic Abundances as Records of Stellar Evolution and Nucleosynthesis*, ed. T. G. Barnes, III & F. N. Bash, 321
- Hollek, J. K., Frebel, A., Roederer, I. U., et al. 2011, *ApJ*, 742, 54
- Holtzman, J. A., Shetrone, M., Johnson, J. A., et al. 2015, *AJ*, 150, 148
- Huber, D., Ireland, M. J., Bedding, T. R., et al. 2012, *ApJ*, 760, 32
- Jofré, E., Petrucci, R., Saffe, C., et al. 2015, *A&A*, 574, A50
- Johnson, D. R. H., & Soderblom, D. R. 1987, *AJ*, 93, 864
- Kaempf, T. A., de Boer, K. S., & Altmann, M. 2005, *A&A*, 432, 879
- Kordopatis, G., Wyse, R. F. G., Gilmore, G., et al. 2015, *A&A*, 582, A122
- Kurucz, R. L. 2011, *Canadian Journal of Physics*, 89, 417
- Kurucz, R. L., Furenlid, I., Brault, J., & Testerman, L. 1984, *Solar flux atlas from 296 to 1300 nm*
- Laney, C. D., Joner, M. D., & Pietrzyński, G. 2012, *MNRAS*, 419, 1637
- Lawler, J. E., Guzman, A., Wood, M. P., Sneden, C., & Cowan, J. J. 2013, *ApJS*, 205, 11
- Lawler, J. E., Sneden, C., Nave, G., et al. 2017, *ApJS*, 228, 10
- Lee, Y. S., Beers, T. C., An, D., et al. 2011, *ApJ*, 738, 187
- Lindgren, L., Lammers, U., Bastian, U., et al. 2016, *A&A*, 595, A4
- Liu, C., & van de Ven, G. 2012, *MNRAS*, 425, 2144
- Liu, Y., Sato, B., Takeda, Y., Ando, H., & Zhao, G. 2010, *PASJ*, 62, 1071
- Lobel, A. 2008, in *Journal of Physics Conference Series*, Vol. 130, *Journal of Physics Conference Series*, 012015
- Lobel, A. 2011, *Canadian Journal of Physics*, 89, 395
- Loebman, S. R., Roškar, R., Debattista, V. P., et al. 2011, *ApJ*, 737, 8
- Luck, R. E. 2015, *AJ*, 150, 88
- Majewski, S. R., APOGEE Team, & APOGEE-2 Team. 2016, *Astronomische Nachrichten*, 337, 863
- Martig, M., Rix, H.-W., Silva Aguirre, V., et al. 2015, *MNRAS*, 451, 2230
- Matrozi, E., Ryde, N., & Dupree, A. K. 2013, *A&A*, 559, A115
- Moore, C. E., Minnaert, M. G. J., & Houtgast, J. 1966, *The solar spectrum 2935 Å to 8770 Å (National Bureau of Standards Monograph, Washington: US Government Printing Office (USGPO))*
- Nidever, D. L., Bovy, J., Bird, J. C., et al. 2014, *ApJ*, 796, 38
- Nissen, P. E. 2004, *Origin and Evolution of the Elements*, 154
- Nissen, P. E., & Schuster, W. J. 2009, in *IAU Symposium*, Vol. 254, *The Galaxy Disk in Cosmological Context*, ed. J. Andersen, Nordströara, B. m, & J. Bland-Hawthorn, 103–108
- O'Brian, T. R., Wickliffe, M. E., Lawler, J. E., Whaling, W., & Brault, J. W. 1991, *Journal of the Optical Society of America B Optical Physics*, 8, 1185
- Ramírez, I., & Meléndez, J. 2005, *ApJ*, 626, 465
- Reddy, B. E., Lambert, D. L., & Allende Prieto, C. 2006, *MNRAS*, 367, 1329
- Reddy, B. E., Tomkin, J., Lambert, D. L., & Allende Prieto, C. 2003, *MNRAS*, 340, 304
- Roederer, I. U., Preston, G. W., Thompson, I. B., et al. 2014, *AJ*, 147, 136
- Roederer, I. U., Sneden, C., Thompson, I. B., Preston, G. W., & Shectman, S. A. 2010, *ApJ*, 711, 573
- Rose, J. A. 1985, *AJ*, 90, 787
- Rosenberg, A., Aparicio, A., Saviane, I., & Piotto, G. 2000a, *A&AS*, 145, 451

- Rosenberg, A., Piotto, G., Saviane, I., & Aparicio, A. 2000b, *A&AS*, 144, 5
- Roškar, R., Debattista, V. P., Quinn, T. R., Stinson, G. S., & Wadsley, J. 2008, *ApJL*, 684, L79
- Ruffoni, M. P., Den Hartog, E. A., Lawler, J. E., et al. 2014, *MNRAS*, 441, 3127
- Salaris, M., & Cassisi, S. 2006, *Evolution of Stars and Stellar Populations*
- Sánchez-Blázquez, P., Peletier, R. F., Jiménez-Vicente, J., et al. 2006, *MNRAS*, 371, 703
- Sandage, A., & Fouts, G. 1987, *AJ*, 93, 74
- Schönrich, R., & Binney, J. 2009, *MNRAS*, 396, 203
- Sellwood, J. A., & Binney, J. J. 2002, *MNRAS*, 336, 785
- Shi, W. B., Chen, Y. Q., Carrell, K., & Zhao, G. 2012, *ApJ*, 751, 130
- Sneden, C. 1973, *ApJ*, 184, 839
- Sneden, C., & Lawler, J. E. 2008, in *American Institute of Physics Conference Series*, Vol. 990, *First Stars III*, ed. B. W. O’Shea & A. Heger, 90–103
- Soubiran, C., Le Campion, J.-F., Brouillet, N., & Chemin, L. 2016, *A&A*, 591, A118
- Stanek, K. Z., Zaritsky, D., & Harris, J. 1998, *ApJL*, 500, L141
- Straižys, V., Zdanavičius, J., Zdanavičius, K., et al. 2005, *Baltic Astronomy*, 14, 555
- Strassmeier, K. G., & Schordan, P. 2000, *Astronomische Nachrichten*, 321, 277
- Takeda, Y., Sato, B., & Murata, D. 2008, *PASJ*, 60, 781
- Tautvaišienė, G. 1996, *Astronomische Nachrichten*, 317, 29
- . 1997, *MNRAS*, 286, 948
- Tautvaišienė, G., Edvardsson, B., Tuominen, I., & Ilyin, I. 2001, *A&A*, 380, 578
- Tody, D. 1993, in *Astronomical Society of the Pacific Conference Series*, Vol. 52, *Astronomical Data Analysis Software and Systems II*, ed. R. J. Hanisch, R. J. V. Brissenden, & J. Barnes, 173
- Tull, R. G. 1998, in *Proc. SPIE*, Vol. 3355, *Optical Astronomical Instrumentation*, ed. S. D’Odorico, 387–398
- Tull, R. G., MacQueen, P. J., Sneden, C., & Lambert, D. L. 1995, *PASP*, 107, 251
- Udalski, A. 2000, *ApJL*, 531, L25
- van Leeuwen, F. 2007, *A&A*, 474, 653
- Venn, K. A., Irwin, M., Shetrone, M. D., et al. 2004, *AJ*, 128, 1177
- Wallace, L., Hinkle, K. H., Livingston, W. C., & Davis, S. P. 2011, *ApJS*, 195, 6
- Wallerstein, G., & Helfer, H. L. 1959, *ApJ*, 129, 720
- Wang, L., Liu, Y., Zhao, G., & Sato, B. 2011, *PASJ*, 63, 1035
- Weistrop, D. 1983, *Bulletin d’Information du Centre de Données Stellaires*, 24, 91
- Wenger, M., Ochsenein, F., Egret, D., et al. 2000, *A&AS*, 143, 9
- Wood, M. P., Lawler, J. E., Sneden, C., & Cowan, J. J. 2013, *ApJS*, 208, 27
- . 2014b, *ApJS*, 211, 20

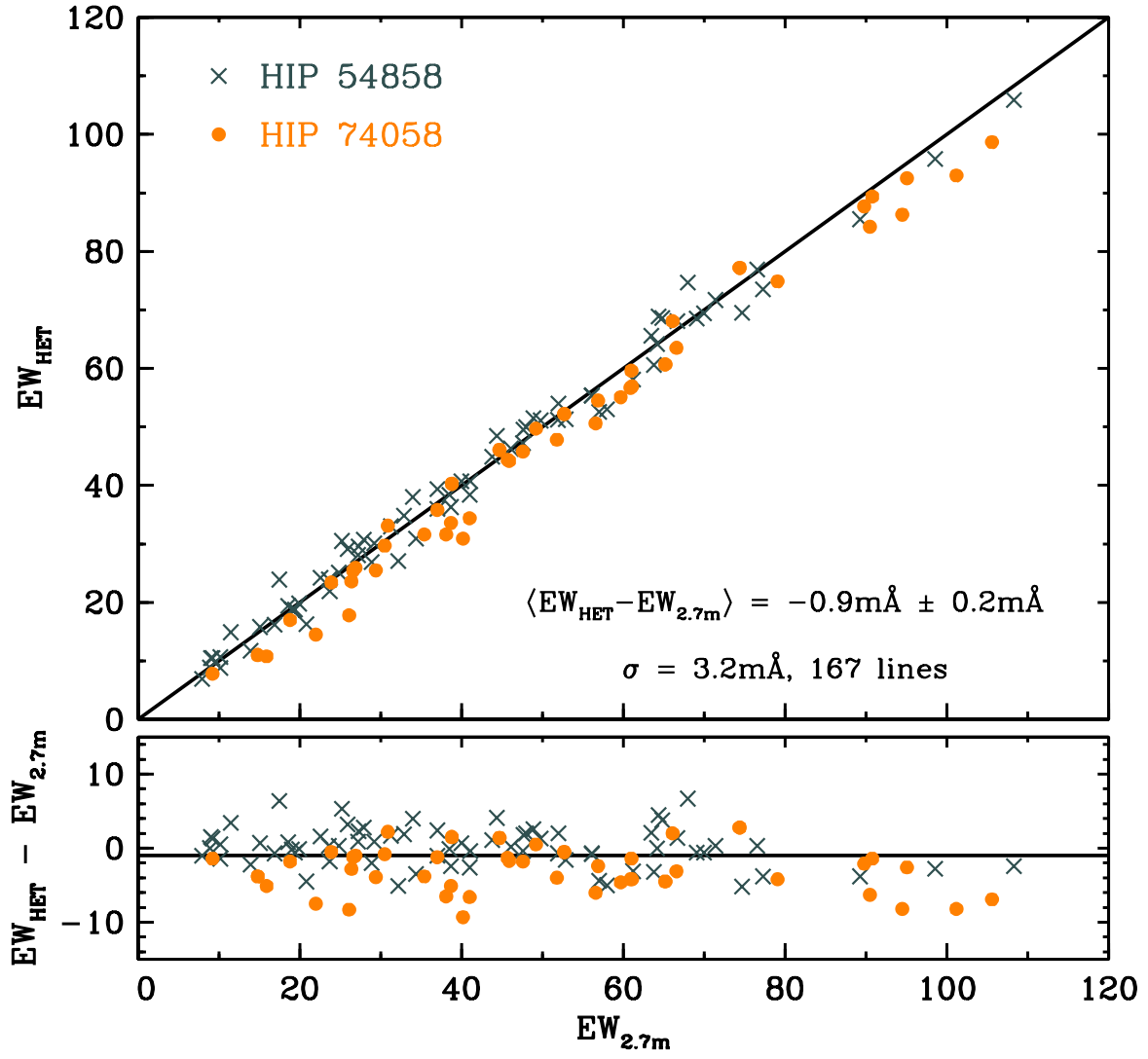


Figure 1. Comparison of equivalent widths for HIP 54858 and HIP 74058 measured on spectra obtained with the 2.7m telescope ($EW_{2.7}$) and the HET (EW_{HET}). In each panel the black line denotes equality of the EW measurements.

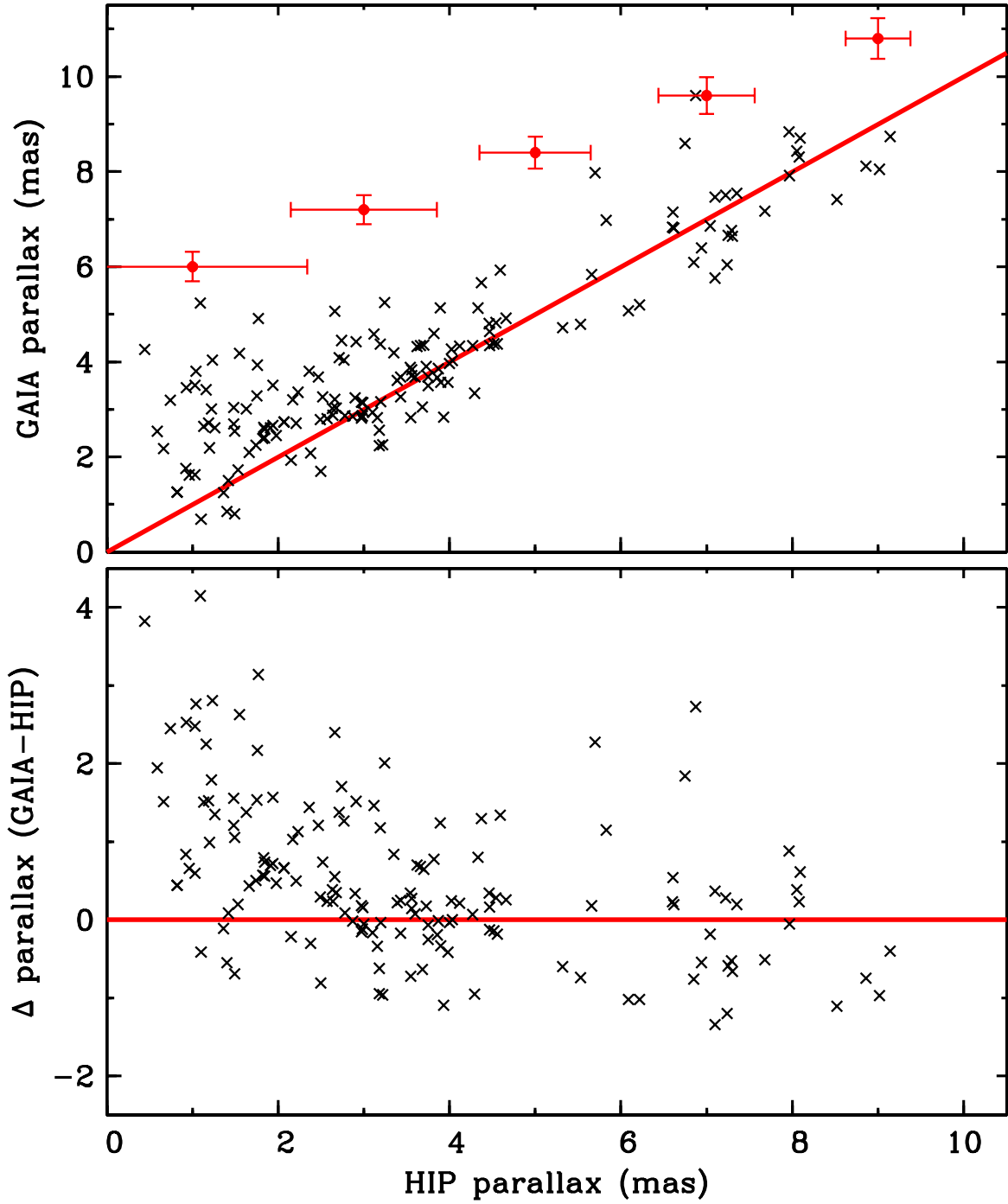


Figure 2. Comparison of parallaxes obtained by Hipparcos [van Leeuwen \(2007\)](#) and Gaia [Lindgren et al. \(2016\)](#). The red lines denote perfect agreement between the two datasets. In the top panel mean uncertainties in the Hipparcos and Gaia parallaxes are shown for the Hipparcos values in bins 2 mas wide, centered at 1, 3, 5, 7, and 9 mas.

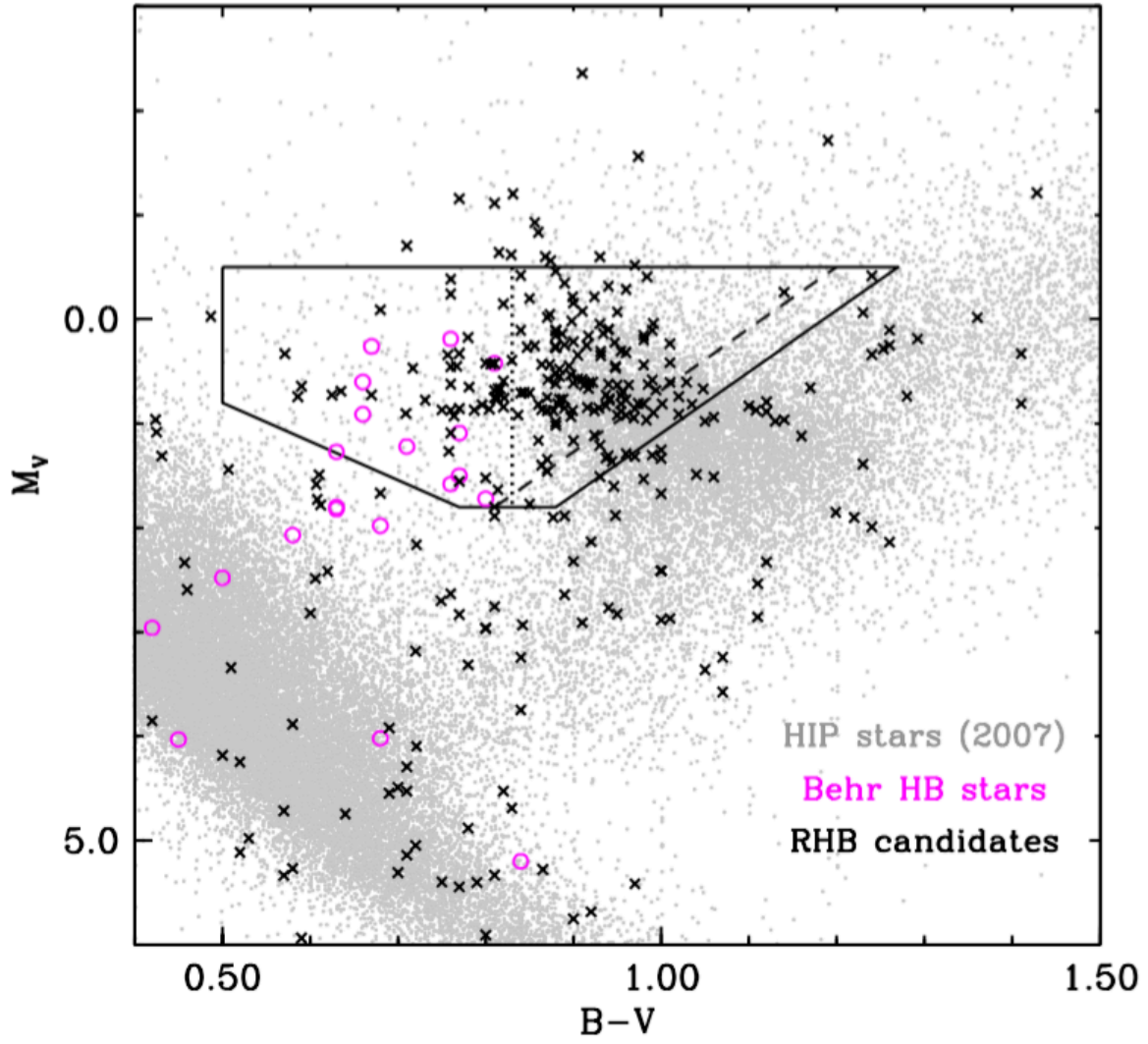


Figure 3. A color-magnitude diagram for the program stars. This figure is adapted from Figure 1 of [Kaempf et al. \(2005\)](#). The solid, and broken lines that [Kaempf et al.](#) used to define the RHB domain are reproduced in the present figure; see the text for a detailed description. The black crosses are from Table-1 data, the gray points are from the revised Hipparcos catalog ([van Leeuwen 2007](#)), and the magenta circles are from a targeted HB spectroscopic study by [Behr \(2003\)](#).

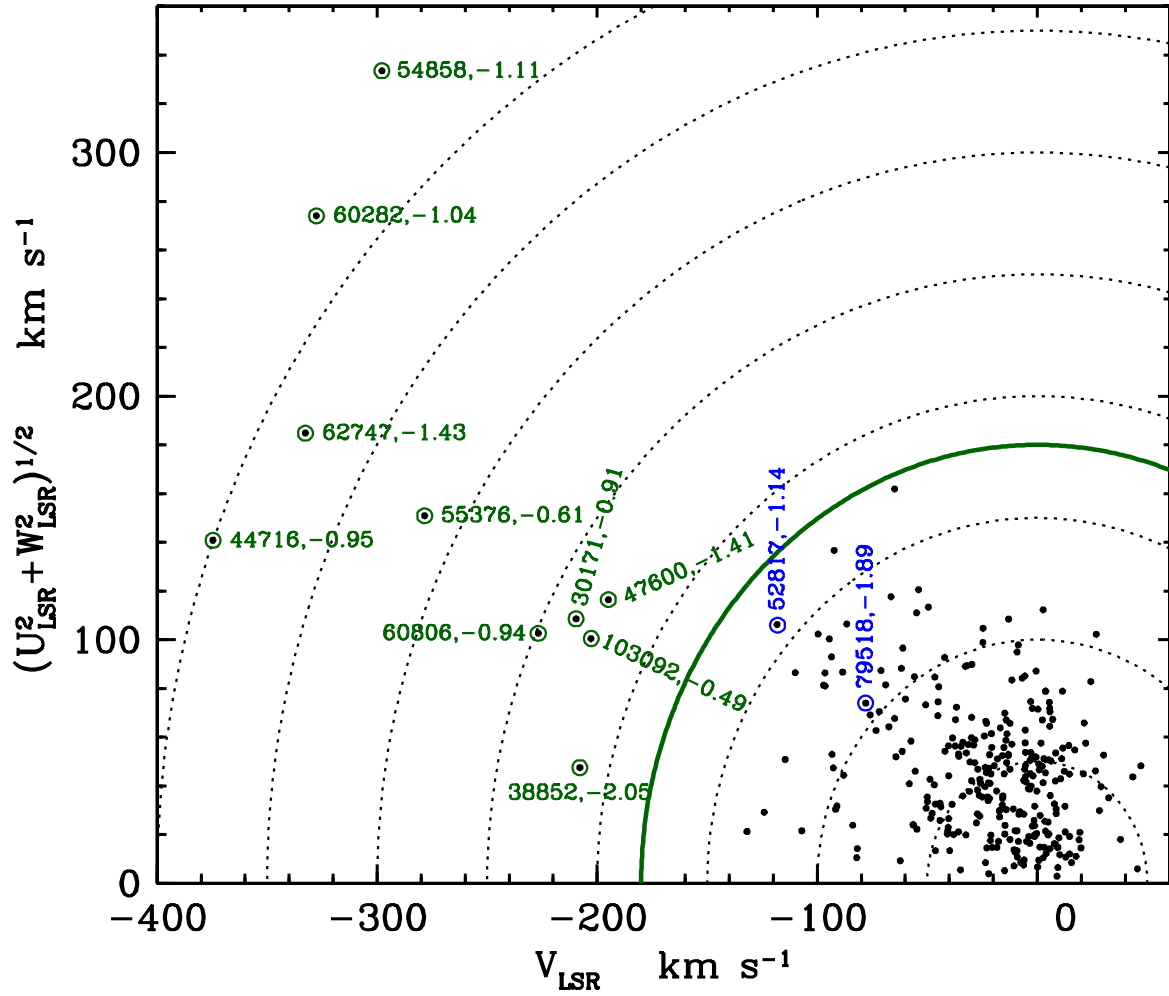


Figure 4. A Toomre diagram for all program stars. The dotted curves are placed at V_{tot} intervals of 50 km s^{-1} . The solid green curve is placed at $V_{\text{tot}} = 180 \text{ km s}^{-1}$, the approximate disk/halo transition velocity. Stars with $V_{\text{tot}} > 180 \text{ km s}^{-1}$ are labeled and two stars with smaller V_{tot} but $[\text{Fe}/\text{H}] < -1$ are labeled in blue (thick disk members) with their Hipparcos names and metallicities from Table 3.

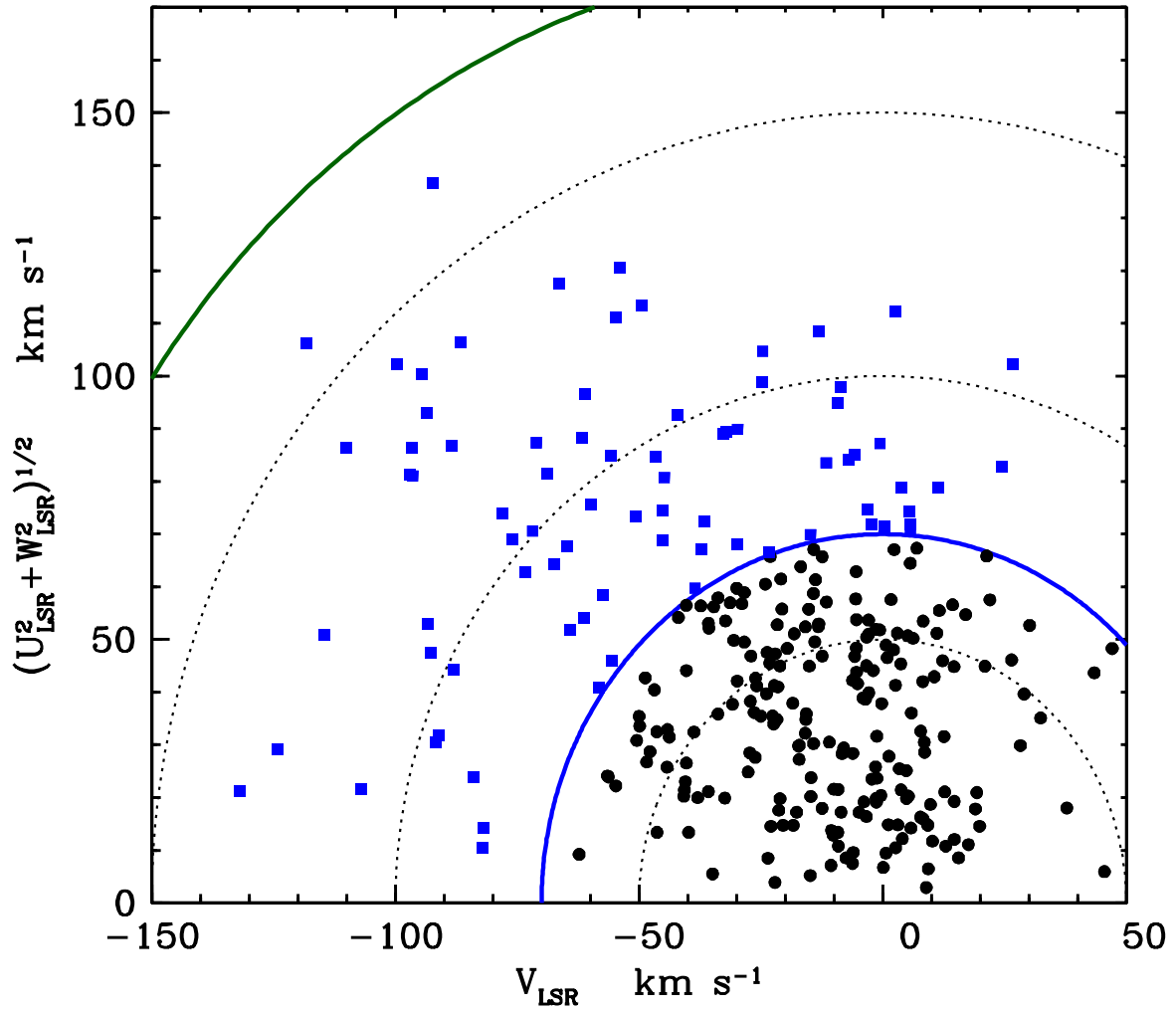


Figure 5. A Toomre diagram for only program stars with $V_{\text{tot}} < 180 \text{ km s}^{-1}$. The dotted curves are lines of constant total velocities (V_{tot}) with intervals of 50 km s^{-1} . The solid green line is as in Figure 4. The solid blue line denotes the estimated approximate upper velocity limit ($V_{\text{tot}} = 70 \text{ km s}^{-1}$) for kinematically-defined thin disk stars (shown with black dots). The thick disk stars are shown with blue squares.

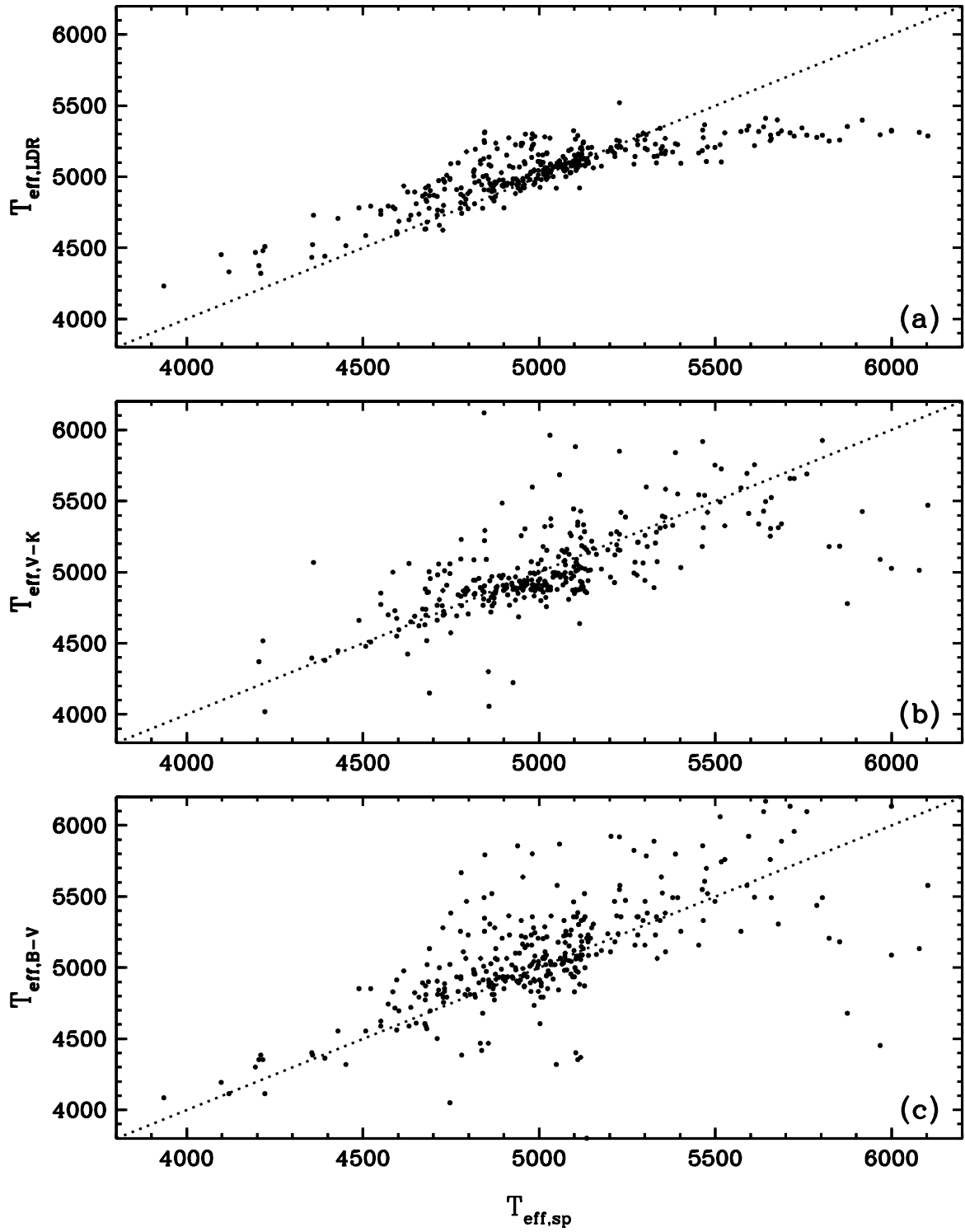


Figure 6. Comparison of final $T_{\text{eff,spec}}$ values derived from spectroscopic analyses with three input T_{eff} indicators.

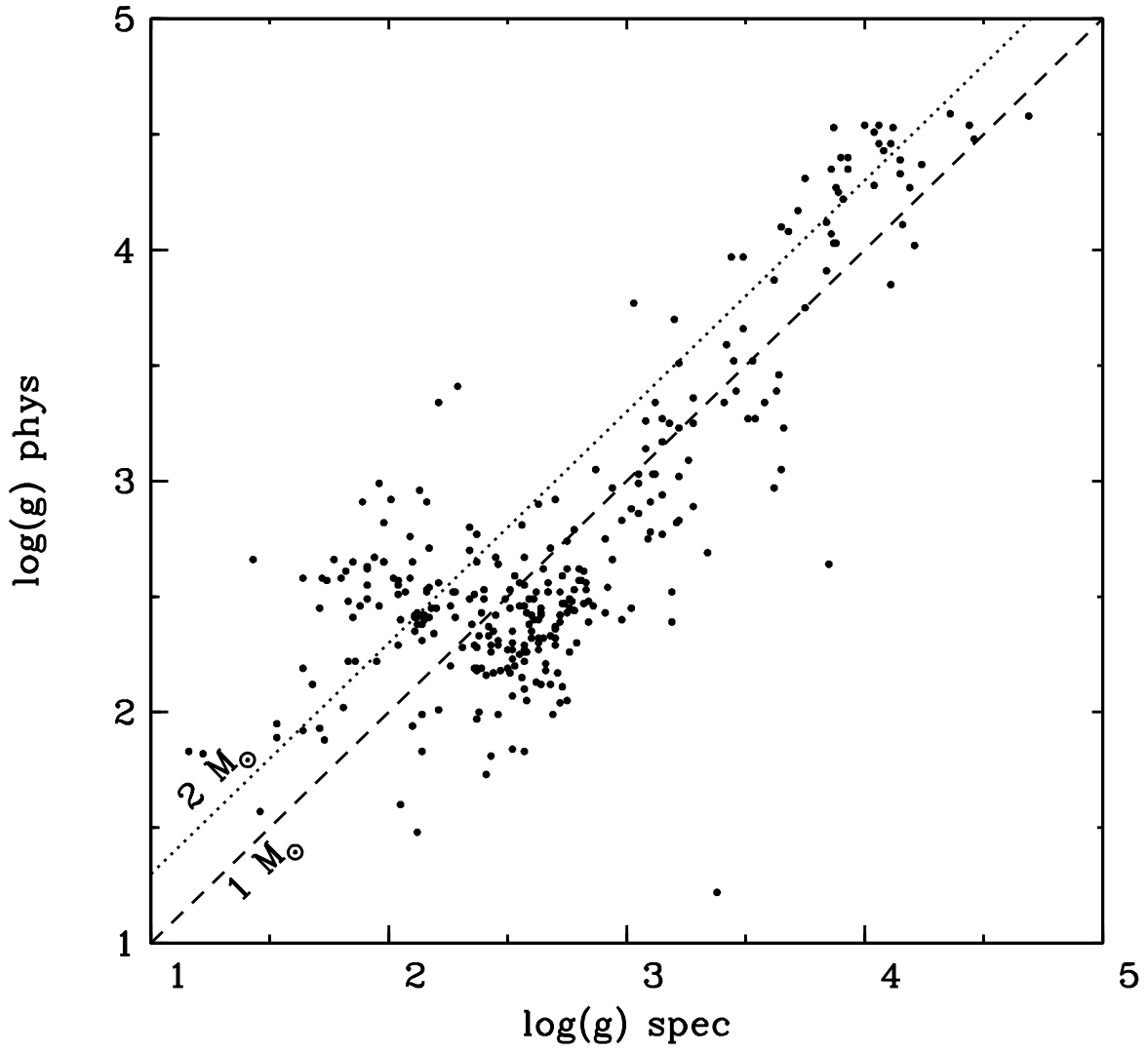


Figure 7. Comparison of final $\log g_{\text{spec}}$ values derived from spectroscopic analyses with the “physical” ones based on photometric and parallax data, and assumed solar masses, $M \equiv 1 M_{\odot}$. Equality of the $\log g$ values is indicated with the dashed line. The change in $\log g_{\text{spec}}$ that would occur if we had assumed $M \equiv 2 M_{\odot}$ is indicated with the dotted line.

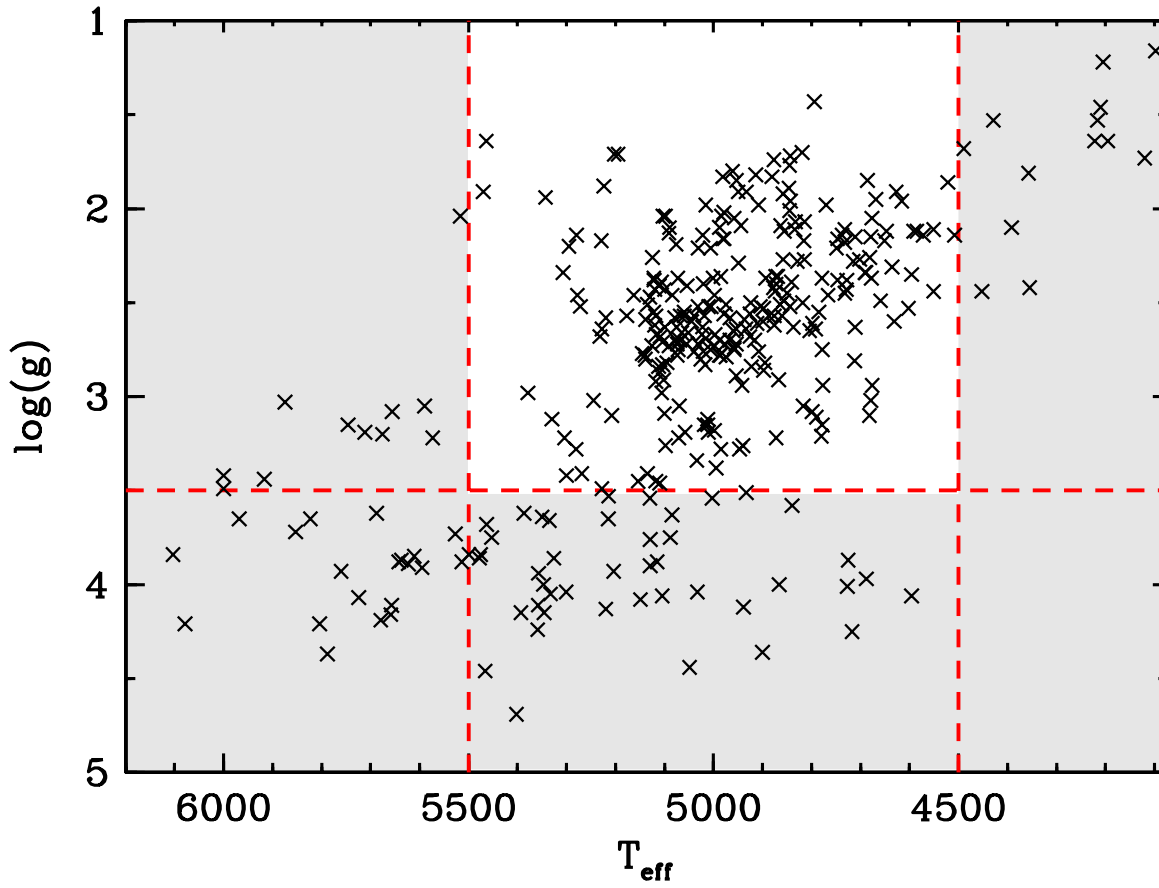


Figure 8. A $T_{\text{eff}} - \log g$ HR diagram for the program stars. The data are taken from Table 3. Gray-shaded areas of the plot, those with $T_{\text{eff}} > 5500$ K or $\log g > 3.5$ are those regions with stars unlikely to be true RHB stars, and thus are of less interest in this study; see text for further discussion.

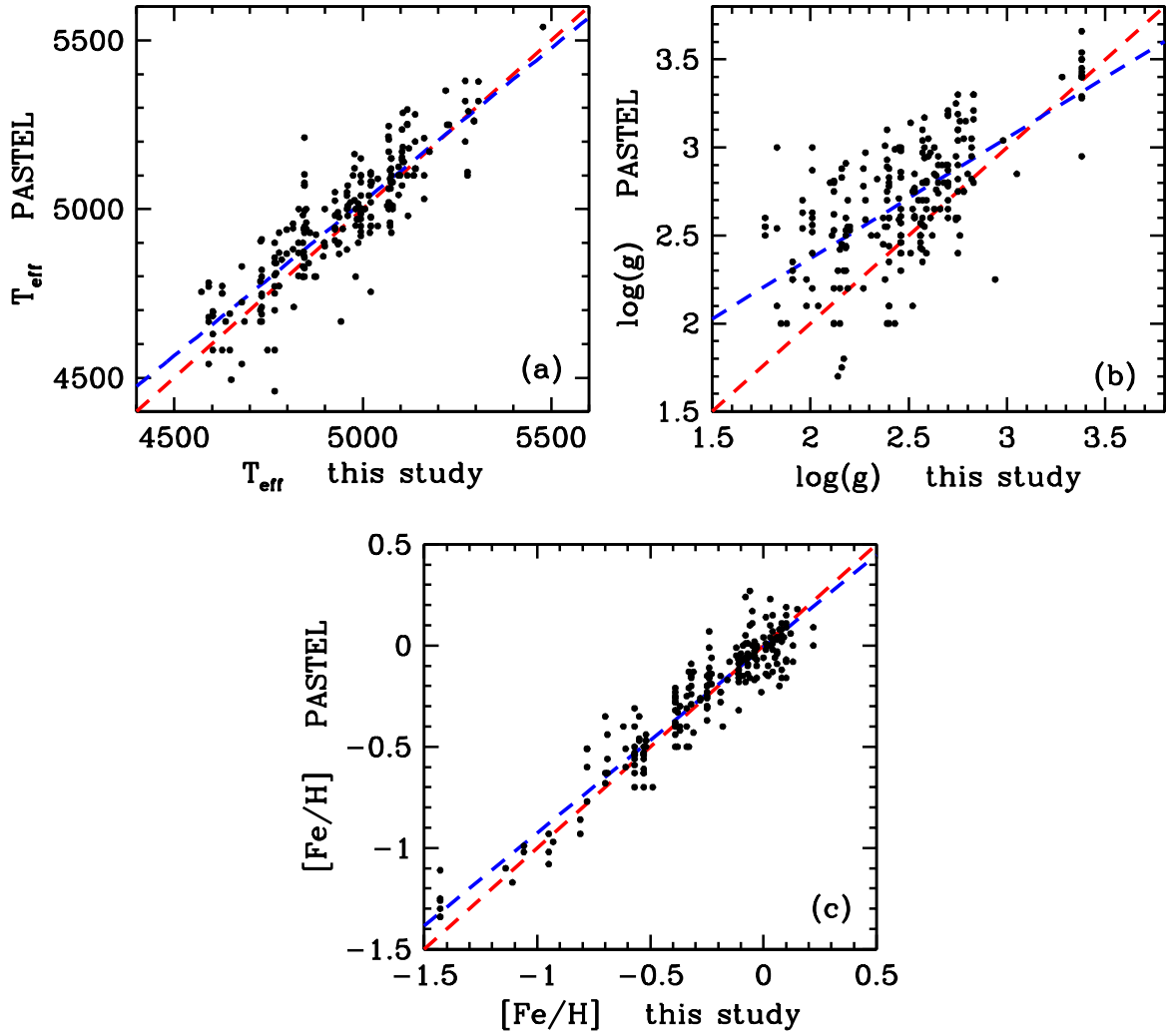


Figure 9. Comparisons of model parameters derived in this paper with ones in the PASTEL catalog (Soubiran et al. 2016). In each panel the red solid line represents equality of the quantities, and the blue dashed line represents the mean offset from equality.

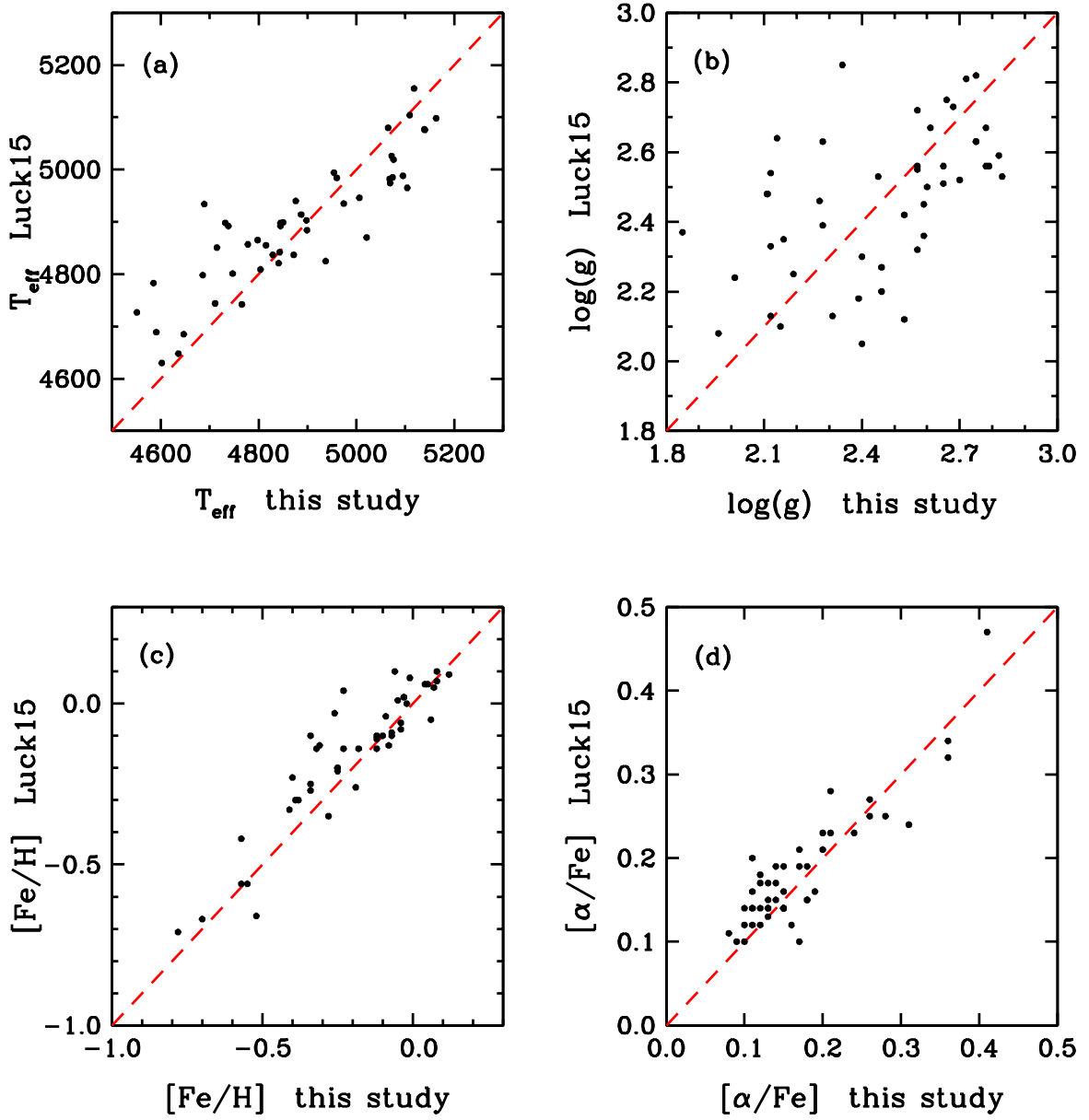


Figure 10. Comparisons of model parameters derived in this paper and $[\alpha/\text{Fe}]$ abundance ratios with ones in Luck (2015). In each panel the red solid line represents equality of the quantities.

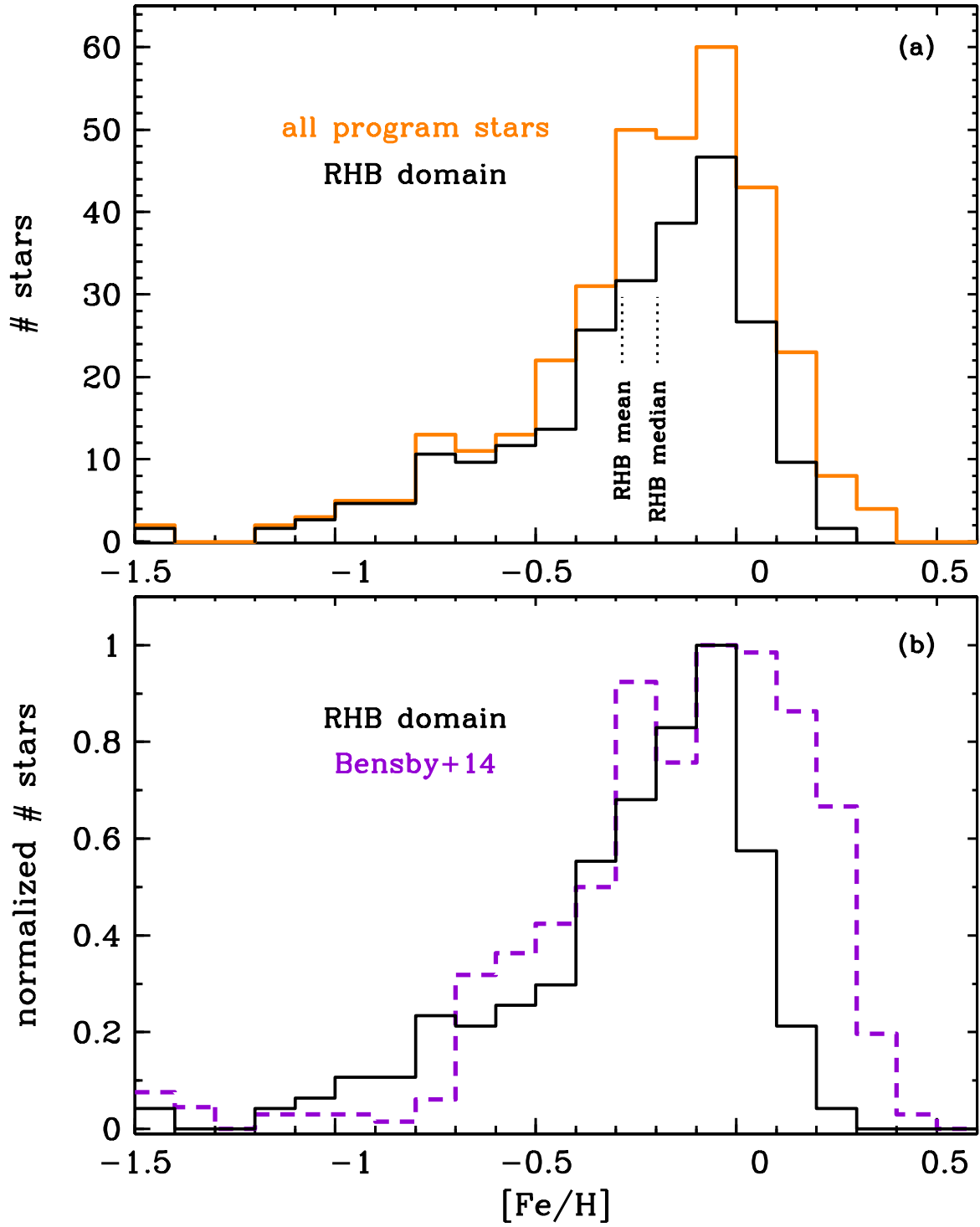


Figure 11. Histograms of the [Fe/H] metallicity distribution of our program stars. The orange “all stars” line is for our total stellar sample. The black “RHB domain” line is for the subset of stars with a reasonable chance to be RHB stars, as defined in Figure 8. Dashed (purple) line represents the sample from [Bensby et al. \(2014\)](#).

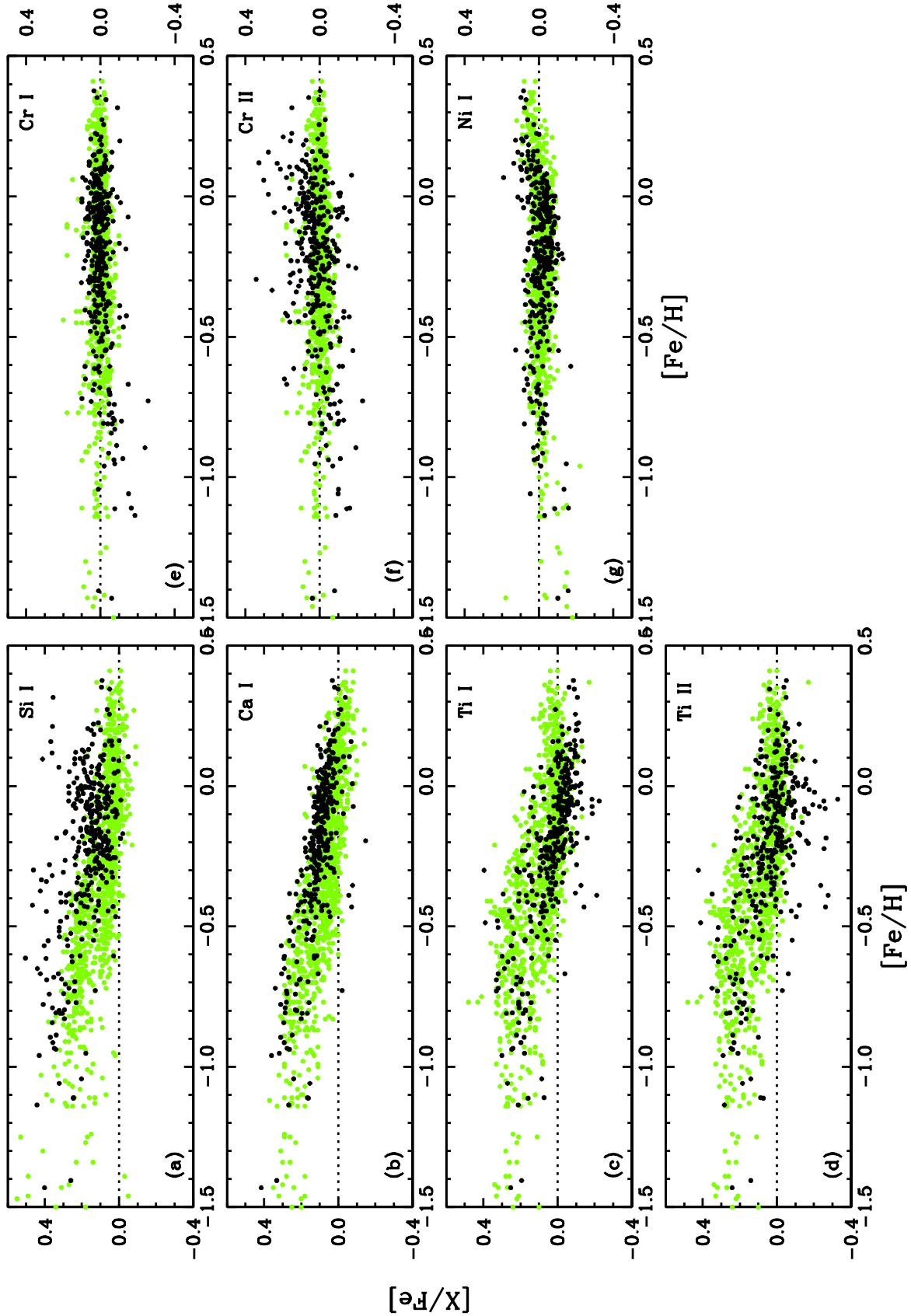


Figure 12. Correlations of $[\text{Fe}/\text{H}]$ metallicity with relative abundance ratios $[\text{X}/\text{Fe}]$ of elements studied in this paper. Black points are our results, and chartreuse points are taken from surveys of Galactic disk main sequence and early subgiants studied by Reddy et al. (2003, 2006) and Bensby et al. (2014). The dotted lines represent the solar abundance ratios, $[\text{X}/\text{Fe}] = 0$.

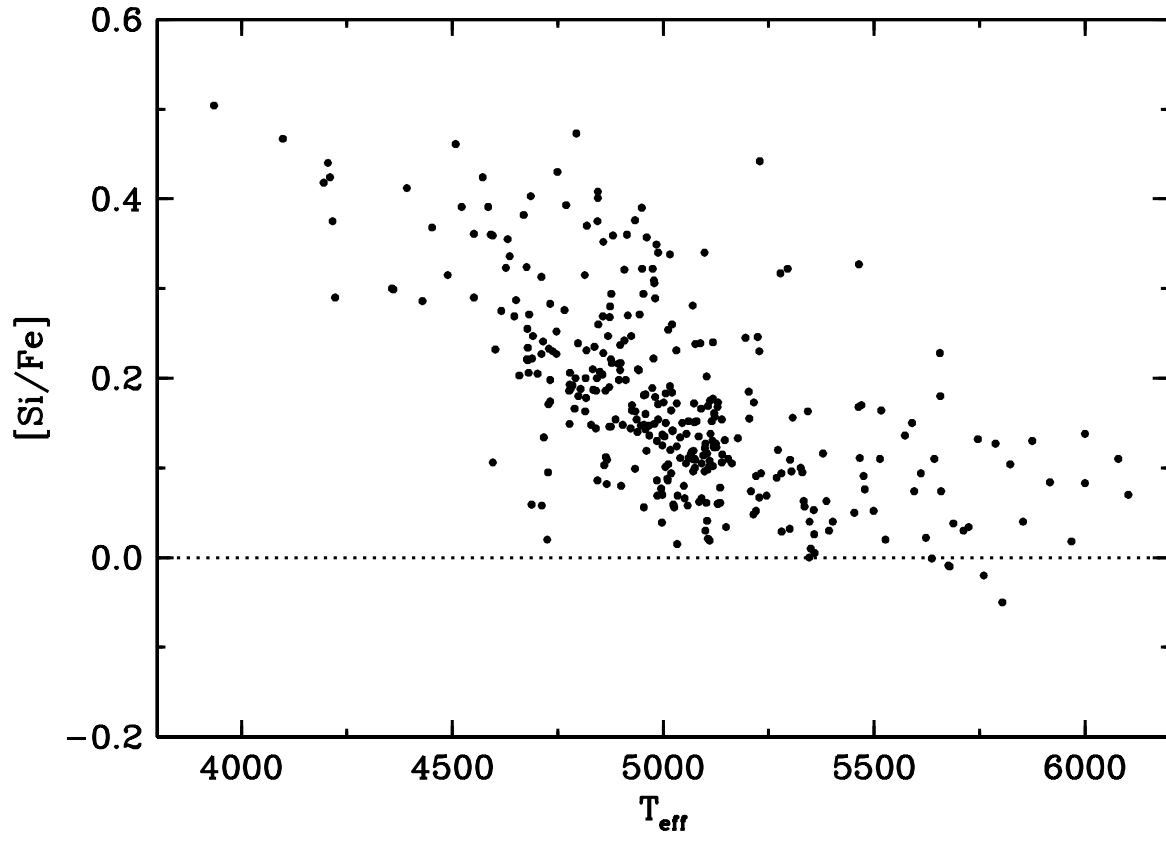


Figure 13. $[\text{Si}/\text{Fe}]$ ratios plotted as a function of T_{eff} .

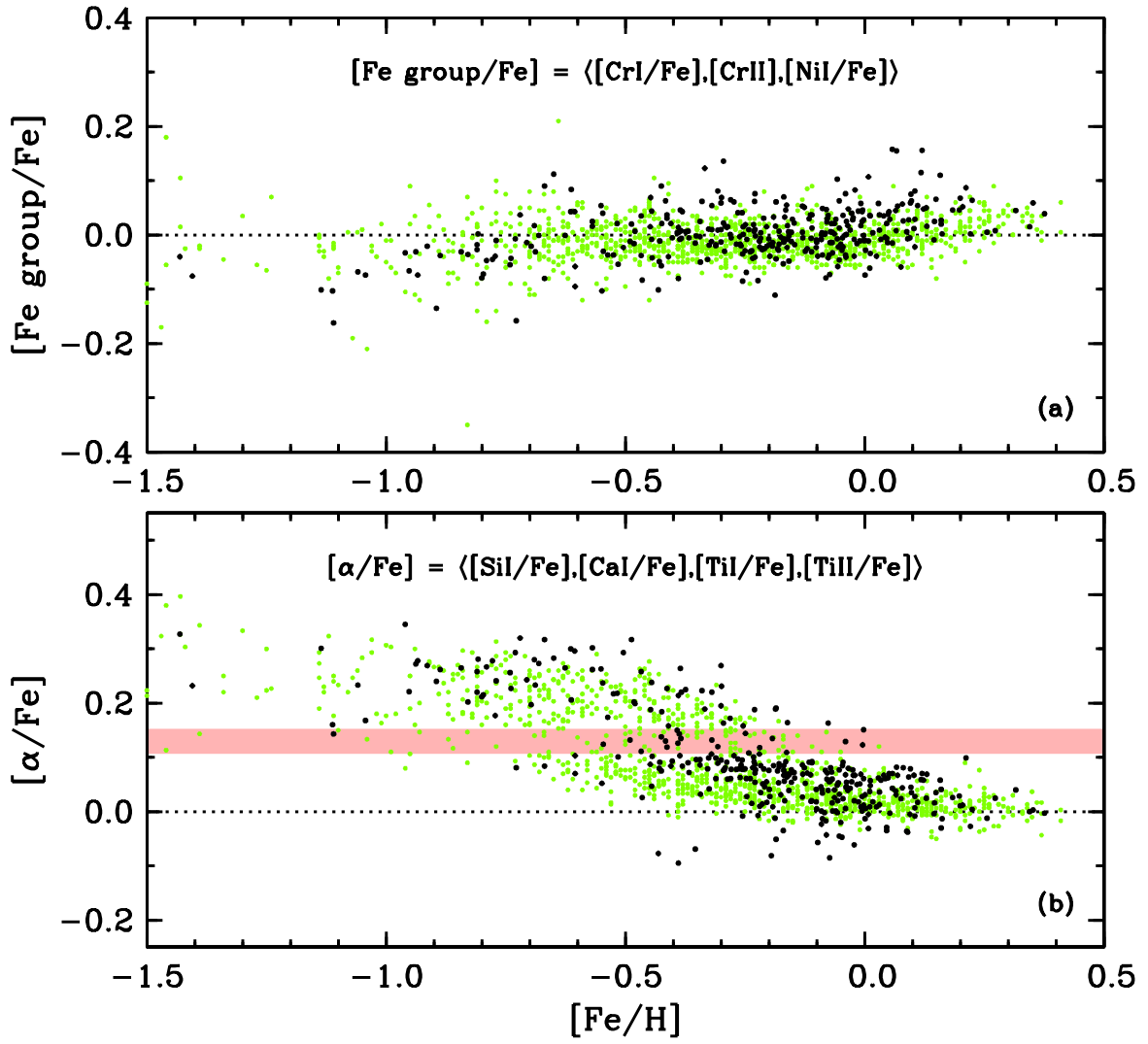


Figure 14. Correlations of $[\text{Fe}/\text{H}]$ with $[\text{X}/\text{Fe}]$ for elements of the Fe group (panel a) and the α 's (panel b) studied in this paper. The species participating in the means are labeled in the figure. The point types and black dotted lines are as in Figure 12. In panel (b) a pale red line has been placed at $[\alpha/\text{Fe}] = +0.13$, the approximate abundance-based dividing line for the α -enhanced group.

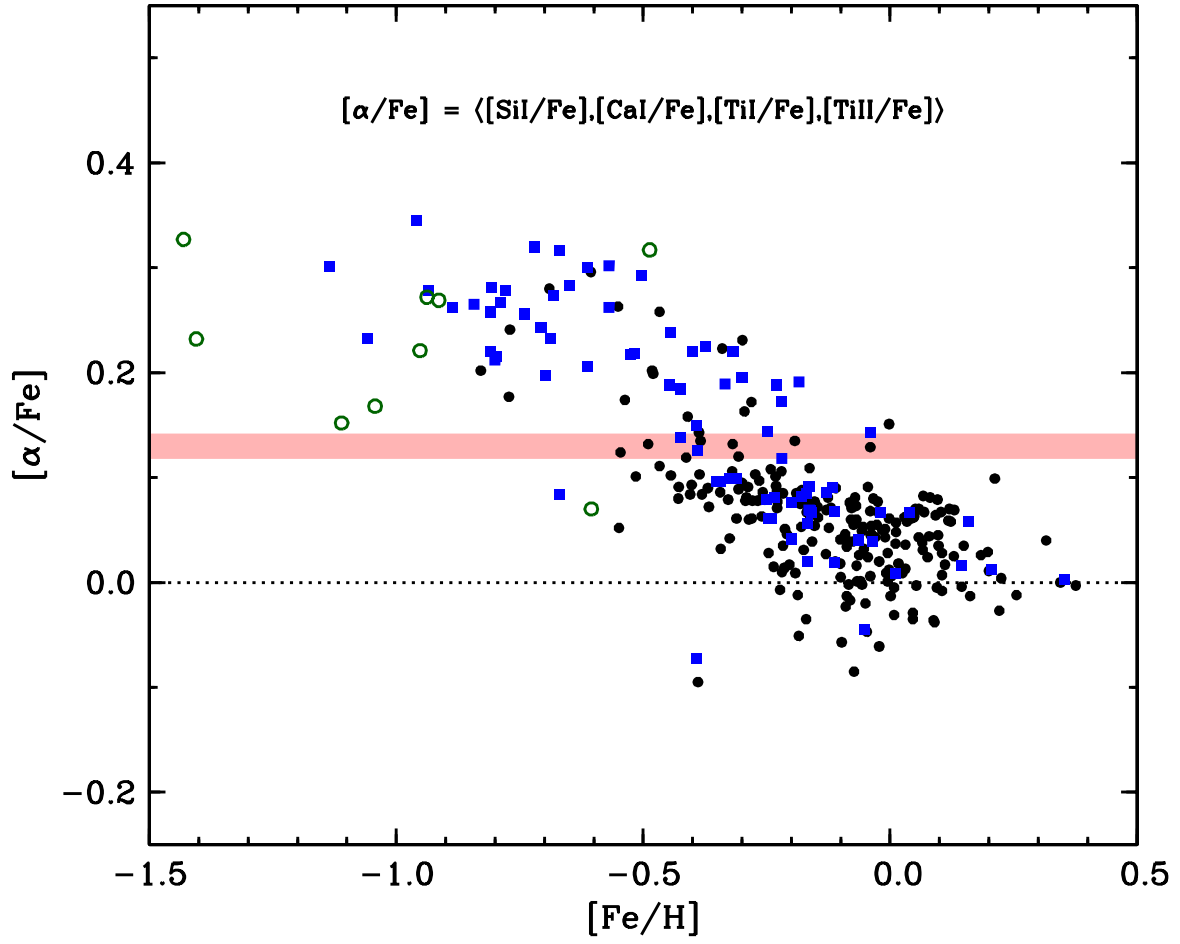


Figure 15. Figure 14 replotted with kinematic group color-coding. The symbols and colors are the same as given in Figure 5. Halo stars are denoted with empty green circles, as in Figure 4.

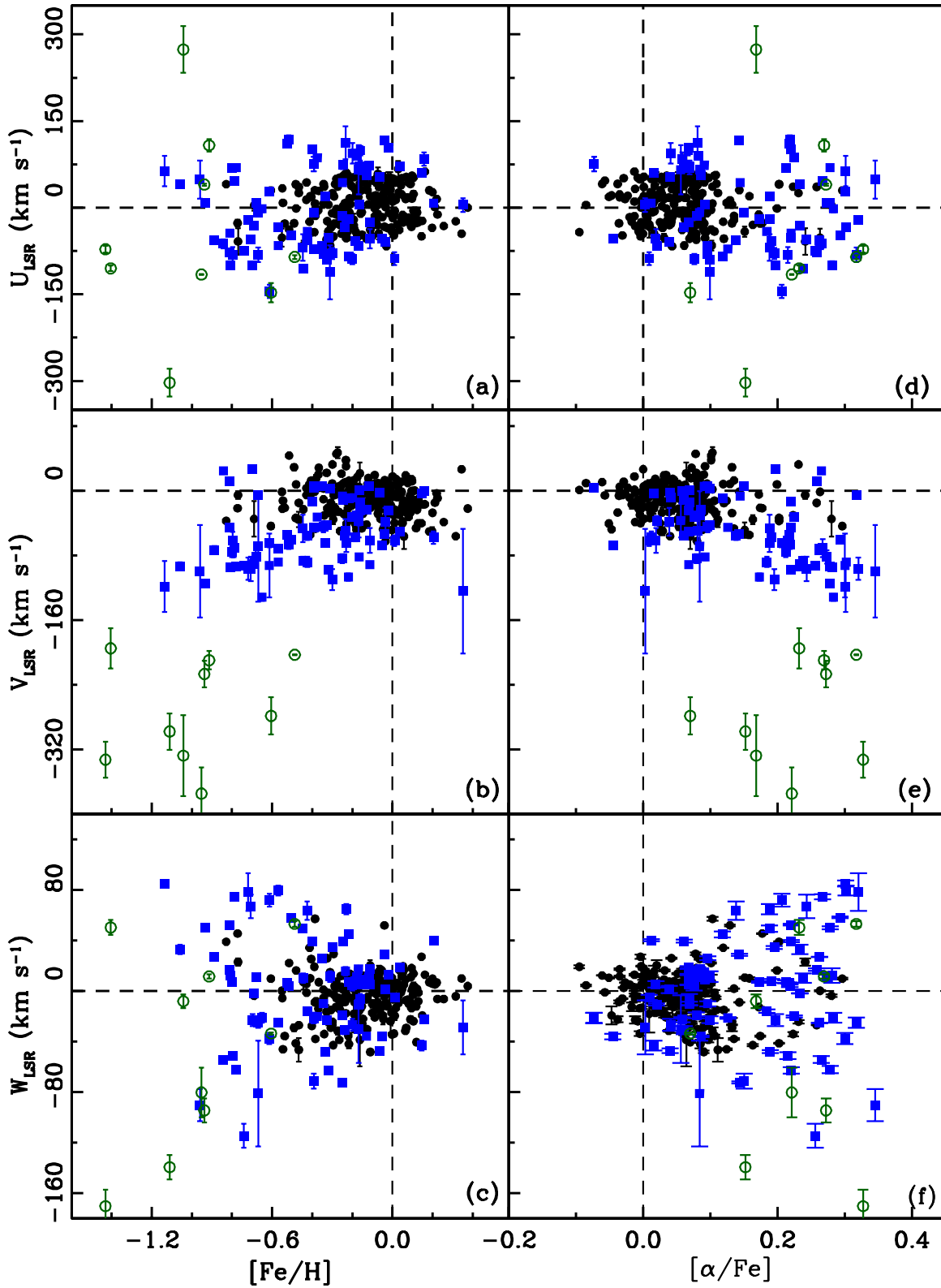


Figure 16. Correlation of $[\text{Fe}/\text{H}]$ with (a) U_{LSR} , (b) V_{LSR} , (c) W_{LSR} , and correlation of $[\alpha/\text{Fe}]$ abundance ratios with (d) U_{LSR} , (e) V_{LSR} , and (f) W_{LSR} . The symbols and colors are the same as in Figure 15.

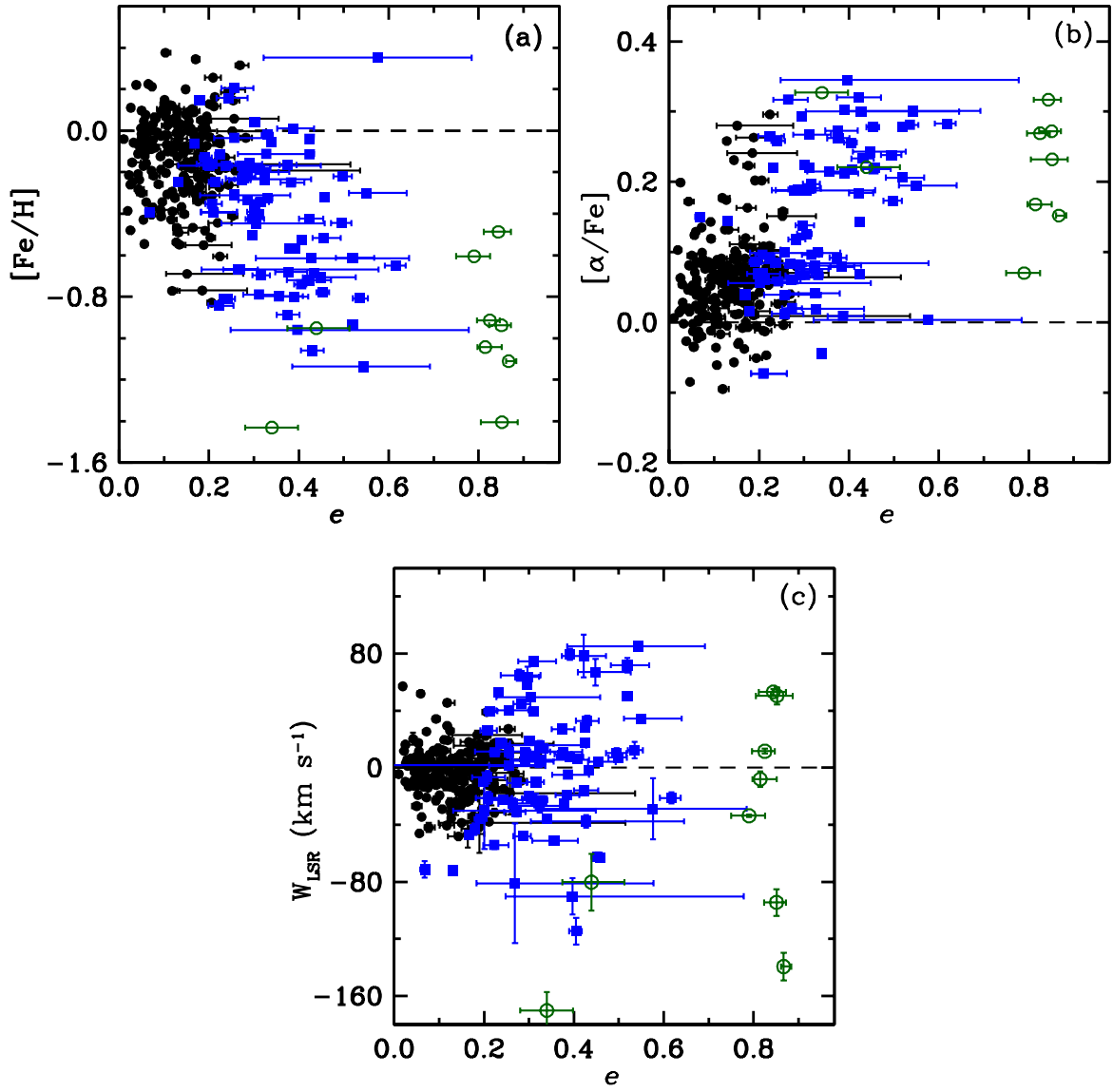


Figure 17. Galactic orbital eccentricity, e , versus (a) $[Fe/H]$, (b) $[\alpha/Fe]$, and (c) W_{LSR} . The symbols and colors are the same as in Figure 15.

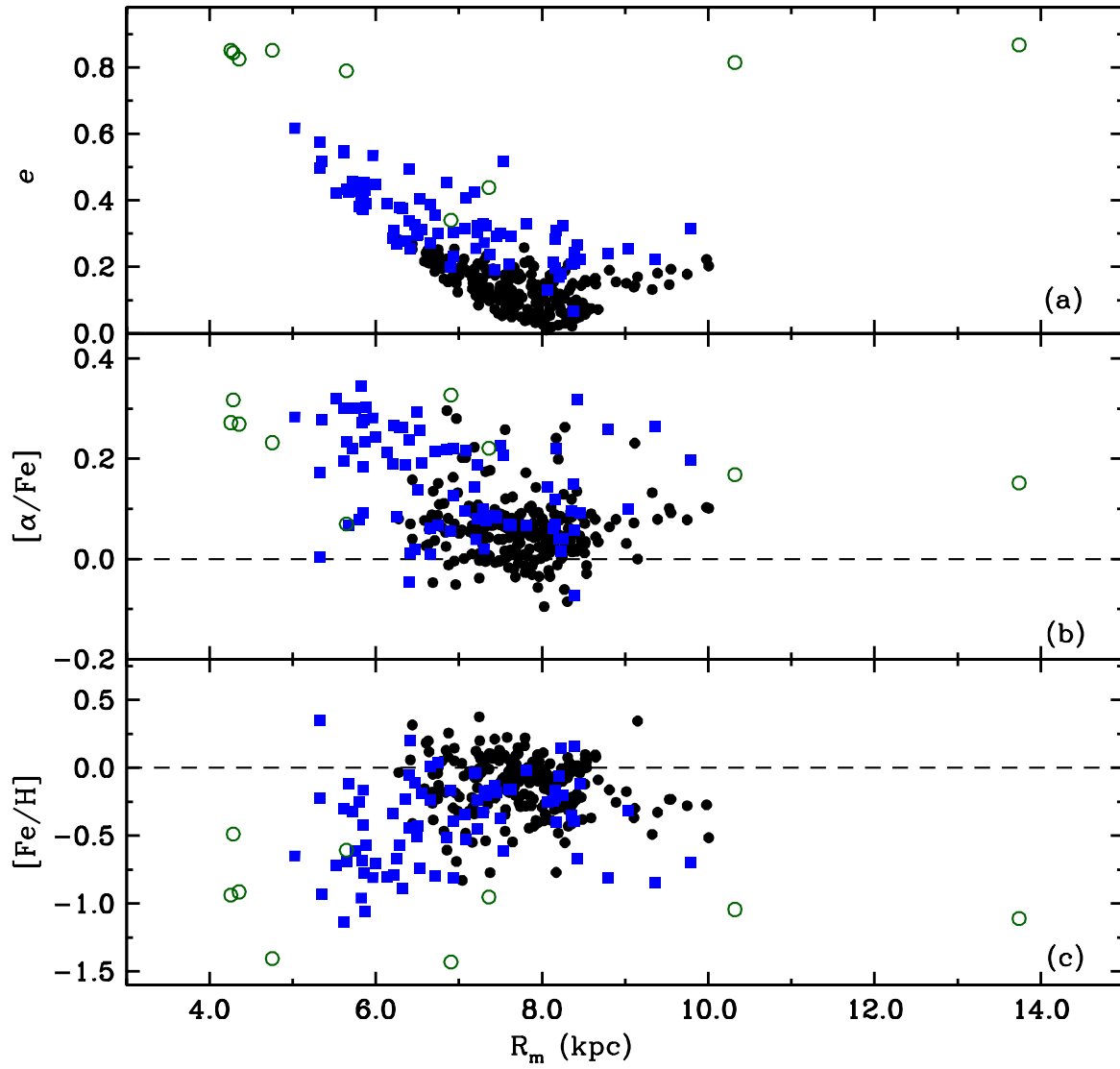


Figure 18. e , $[\alpha/\text{Fe}]$ and $[\text{Fe}/\text{H}]$ plotted as a function of R_m (mean distance to the Galactic center). The symbols and colors are the same as in Figure 15.

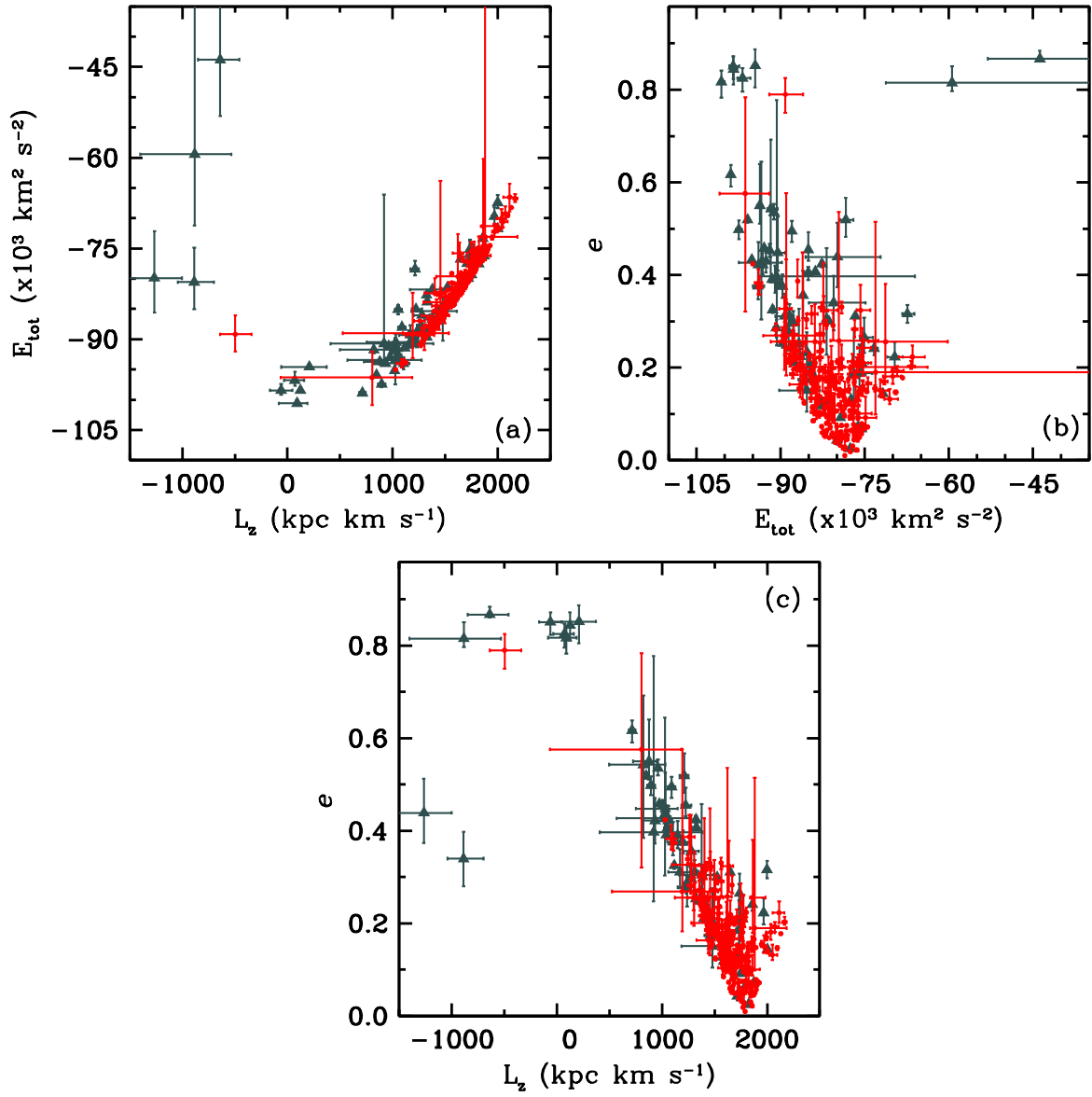


Figure 19. (a) $E_{\text{tot}} - L_z$. (b) $e - E_{\text{tot}}$, and (c) $e - L_z$ relations for the whole sample, including two low-metallicity stars with $[\text{Fe}/\text{H}] < -1.5$. Dark grey triangles denote α -rich ($[\alpha/\text{Fe}] > +0.13$), red dots denote α -solar ($[\alpha/\text{Fe}] \lesssim +0.13$) stars.

Table 1. Basic Program Star Data

Star ^a	RA ₂₀₀₀ ^b	Dec ₂₀₀₀ ^b	<i>B</i> ^b	<i>V</i> ^b	<i>K</i> ^b	<i>A_V</i>	ref(<i>A_V</i>)	<i>E(B - V)</i> ^c	spec ^d	inst ^d
HIP 258	00 03 13.32	+17 33 08.16	7.69	6.57	4.36				K0	2.7m/Tull
HIP 410	00 05 01.19	+27 40 29.22	7.41	6.48	4.27				G8III	2.7m/Tull
HIP 476	00 05 41.96	+13 23 46.56	6.43	5.55	3.77				G5III	2.7m/Tull
HIP 716	00 08 52.14	+25 27 46.74	7.22	6.25	4.20				K0III	2.7m/Tull
HIP 1009	00 12 34.17	+44 42 25.90	7.64	6.52	4.51				K0	2.7m/Tull
...										

References—1 - [Bailer-Jones \(2011\)](#); 2 - [Jofré et al. \(2015\)](#); 3 - [Straižys et al. \(2005\)](#); 4 - [Liu et al. \(2010\)](#); 5 - [Takeda et al. \(2008\)](#); 6 - [Matrozis et al. \(2013\)](#); 7 - [Goswami & Karinkuzhi \(2013\)](#); 8 - [Wang et al. \(2011\)](#); 9 - [Cruzalèbes et al. \(2013\)](#); 10 - [Sánchez-Blázquez et al. \(2006\)](#); 11 - [Huber et al. \(2012\)](#)

^a When available, HIP # preferably, then BD #, then GSC #

^b SIMBAD; spec = spectral type

^c $E(B - V) = A_V/3.1$

^d 2.7m/Tull = McDonald 2.7m telescope and [Tull et al. \(1995\)](#) echelle spectrograph; HET/HRS = Hobby-Eberly Telescope and [Tull \(1998\)](#) echelle spectrograph

(This table is available in its entirety in machine-readable form.)

Table 2. Parallaxes and Velocities

Star	π_{Hip}	err(π_{Hip})	π_{Gaia}	err(π_{Gaia})	<i>RV</i>	σ_{RV}	<i>U_{LRS}</i>	$\sigma_{U_{LRS}}$	<i>V_{LRS}</i>	$\sigma_{V_{LRS}}$	<i>W_{LRS}</i>	$\sigma_{W_{LRS}}$
	mas	mas	mas	mas	km s ⁻¹	km s ⁻¹	km s ⁻¹	km s ⁻¹	km s ⁻¹	km s ⁻¹	km s ⁻¹	km s ⁻¹
HIP 258	5.83	0.42	6.98	0.47	-18.9	0.19	-5.44	1.30	-46.29	2.58	-12.25	2.18
HIP 410	5.95	0.42			14.60	0.14	-49.46	3.91	-15.87	2.30	-17.34	1.17
HIP 476	8.75	0.30			2.31	0.12	-9.55	0.67	-6.04	0.45	-0.80	0.24
HIP 716	7.22	0.32	7.50	0.57	15.05	0.17	-65.43	5.38	2.34	1.08	14.73	1.25
HIP 1009	7.10	0.63	7.47	0.53	-35.55	0.17	-23.54	3.45	-56.28	2.22	-4.16	1.58
...												

^a when available, using π_{Gaia} , else π_{Hip} .

(This table is available in its entirety in machine-readable form.)

Table 3. Model Atmospheric Parameters

Star	<i>T_{eff}</i>	<i>T_{eff}</i>	<i>T_{eff}</i>	log <i>g</i>	log <i>g</i>	<i>T_{eff}</i>	log <i>g</i>	[M/H]	ξ_t	[Fe/H]	σ	# ^a	[Fe/H]	σ	#	[Fe/H]
	(B-V)	(V-K)	(LDR)	(Hip)	(Gaia)	(K)			(km s ⁻¹)	I	I	I	II	II	II	(I, II)
HIP 258	4589	4853	4672	2.19	2.35	4551	2.44	0.01	1.26	0.12	0.07	52	0.12	0.08	8	0.12
HIP 410	4954	4854	5022	2.29		4876	2.57	-0.18	1.15	-0.12	0.06	66	-0.07	0.06	10	-0.10
HIP 476	5068	5329	5117	2.33		5109	2.68	-0.13	1.36	-0.02	0.07	66	0.00	0.04	11	-0.02
HIP 716	4887	5010	4984	2.37	2.41	4732	2.11	-0.41	1.35	-0.28	0.06	65	-0.33	0.04	10	-0.31
HIP 1009	4589	5061	4697	2.30	2.35	4631	2.60	0.20	1.19	0.34	0.08	50	0.31	0.05	9	0.32
...																

^a #: The number of lines contributing to an abundance determination.

(This table is available in its entirety in machine-readable form.)

Table 4. Sensitivity (σ) of elemental abundances to the uncertainties in atmospheric parameters.

Species	$\Delta T_{\text{eff}}(\text{K})$	$\Delta \log g$	$\Delta \xi_t (\text{km s}^{-1})$
	-150/+150	-0.25/+0.25	-0.25/+0.25
Si I	+0.01 / -0.02	-0.03 / +0.03	+0.04 / -0.04
Ca I	-0.13 / +0.14	+0.03 / -0.03	+0.12 / -0.11
Ti I	-0.18 / +0.20	0.00 / 0.00	+0.04 / -0.05
Ti II	+0.03 / -0.02	-0.11 / +0.11	+0.11 / -0.12
Cr I	-0.16 / +0.17	+0.02 / -0.02	+0.09 / -0.08
Cr II	+0.10 / -0.08	-0.10 / +0.11	+0.10 / -0.10
Fe I	-0.12 / +0.11	0.00 / 0.00	+0.11 / -0.11
Fe II	+0.11 / -0.11	-0.12 / +0.12	+0.08 / -0.08
Ni I	-0.09 / +0.07	-0.03 / +0.03	+0.08 / -0.09

Table 5. Elemental Abundances

Star	[Si/Fe]			[Ca/Fe]			[Ti/Fe]			[Ti/Fe]			[Cr/Fe]			[Cr/Fe]			[Ni/Fe]		
	I	σ	# ^a	I	σ	#	I	σ	#	I	σ	#	I	σ	#	I	σ	#	I	σ	#
HIP 258	0.36	0.06	10	0.03	0.06	7	-0.09	0.07	10	-0.06	0.09	5	-0.02	0.07	13	0.23	0.09	4	0.14	0.07	16
HIP 410	0.15	0.06	15	-0.07	0.05	10	-0.05	0.07	11	-0.09	0.11	5	-0.03	0.07	11	-0.03	0.05	5	-0.02	0.07	23
HIP 476	0.10	0.07	13	-0.10	0.05	10	-0.01	0.08	11	-0.01	0.04	5	-0.04	0.08	15	0.00	0.05	5	-0.08	0.06	22
HIP 716	0.17	0.07	16	-0.13	0.05	10	-0.03	0.07	11	-0.03	0.09	5	-0.04	0.05	11	-0.05	0.05	5	-0.06	0.06	24
HIP 1009	0.36	0.05	10	-0.04	0.08	9	-0.11	0.09	11	-0.05	0.05	3	-0.09	0.07	13	-0.15	0.07	3	0.08	0.05	14
...																					

^a #: The number of lines contributing to an abundance determination.

(This table is available in its entirety in machine-readable form.)

Table 6. Galactic Orbital Parameters

Star	L_z (kpc km s $^{-1}$)	E_{tot} (km 2 s $^{-2}$)	R_m (kpc)	e
HIP 258	1394.9 $^{+18.0}_{-20.5}$	-88280.4 $^{+359.9}_{-377.9}$	6.64 $^{+0.10}_{-0.14}$	0.211 $^{+0.014}_{-0.009}$
HIP 410	1636.7 $^{+18.8}_{-17.1}$	-81144.0 $^{+256.7}_{-176.4}$	7.62 $^{+0.13}_{-0.16}$	0.180 $^{+0.014}_{-0.013}$
HIP 476	1715.8 $^{+2.7}_{-3.6}$	-80595.7 $^{+63.3}_{-86.9}$	7.75 $^{+0.04}_{-0.04}$	0.050 $^{+0.003}_{-0.003}$
HIP 716	1781.0 $^{+8.4}_{-11.0}$	-76473.0 $^{+201.7}_{-148.2}$	8.32 $^{+0.19}_{-0.17}$	0.207 $^{+0.016}_{-0.013}$
HIP 1009	1315.9 $^{+11.0}_{-17.0}$	-89667.2 $^{+151.4}_{-237.5}$	6.44 $^{+0.10}_{-0.16}$	0.269 $^{+0.019}_{-0.010}$
...				

(This table is available in its entirety in machine-readable form.)